Results in Physics 49 (2023) 106499

Contents lists available at ScienceDirect

Results in Physics

journal homepage: www.elsevier.com/locate/rinp

Joint experimental and theoretical study of bulk Y_2O_3 at high pressure

A.L.J. Pereira [a,b,*], J.A. Sans [a], O. Gomis [c], D. Santamaría-Pérez [d], S. Ray [e], A. Godoy-Jr [b], A.S. da Silva-Sobrinho [b], P. Rodríguez-Hernández [f], A. Muñoz [f], C. Popescu [g], F.J. Manjón [a,*]

[a] Instituto de Diseño para la Fabricación y Producción Automatizada, MALTA Consolider Team, Universitat Politècnica de València, 46022 València, Spain
[b] Laboratório de Plasmas e Processos – LPP, Instituto Tecnológico de Aeronáutica – ITA, 12228-900 São José dos Campos, Brazil
[c] Centro de Tecnologías Físicas, MALTA Consolider Team, Universitat Politècnica de València, 46022 Valencia, Spain
[d] Departament de Física Aplicada-ICMUV, MALTA Consolider Team, Universitat de Valencia, Burjassot, Spain
[e] Department of Chemistry, Faculty of Science, Rabindranath Tagore University, Bhopal
[f] Departamento de Física, Instituto de Materiales y Nanotecnología, MALTA Consolider Team, Universidad de La Laguna, 38207 San Cristóbal de La Laguna, Spain
[g] CELLS-ALBA Synchrotron Light Facility, Cerdanyola del Valles, 08290 Barcelona, Spain

ARTICLE INFO

Keywords:
Yttrium oxide
Rare-earth sesquioxides
High-pressure
X-ray diffraction
Raman scattering
Ab initio calculations

ABSTRACT

We report a joint experimental and theoretical study of the structural and vibrational properties of C-type bulk Y_2O_3 under hydrostatic compression. The combination of high-pressure X-ray diffraction and Raman scattering experimental measurements with *ab initio* theoretical calculations on bulk Y_2O_3 allows us to confirm the cubic (C-type) – monoclinic (B-type) – trigonal (A-type) phase transition sequence on the upstroke and the trigonal-monoclinic phase transition on the downstroke. This result reconciles with the results already found in related rare-earth sesquioxides of cations with similar ionic radii as Y, such as Ho_2O_3 and Dy_2O_3, and ends with the controversy regarding the existence of the intermediate monoclinic phase between the cubic and trigonal phases in pure bulk Y_2O_3 on the upstroke. As a byproduct, the good agreement between experimental and calculated results allows us to use extensive theoretical data to discuss the structural and vibrational behavior of the three phases of Y_2O_3 under compression, thus allowing a more detailed understanding of the effect of pressure on rare-earth sesquioxides than previous studies.

Introduction

The family of rare-earth (RE) sesquioxides (SOs), in particular the lanthanide one (Ln_2O_3; *Ln* = La to Lu, Y, and Sc), holds great potential in a wide range of applications, such as light emitters (lasers and improved phosphors), catalysts, high-dielectric constant (high-k) gates, and even solid-state optical quantum memories [1]. Their fundamental properties are linked to the Ln radius that can be finely tuned along the lanthanide family. Yttrium oxide (Y_2O_3) is a multifunctional material that has received a lot of attention from the scientific and technological community due to its non-toxicity, bio-compatibility, and abundance in nature [2]. The interest is even more prominent when Y_2O_3 nanoparticles are doped with other RE elements, such as Tm, Er, and Eu. This interest comes from the strong and well-defined electronic transitions, related to electrons at the 4*f* levels of RE trivalent ions embedded in the Y_2O_3 lattice. These transitions produce strong and stable emissions in specific regions of the electromagnetic spectrum, such as blue (Tm^{3+}), green (Er^{+3}), and red (Eu^{3+}), that are important for several optoelectronic applications, such as high-density optical storage and electroluminescent devices. In Eu^{3+}-doped Y_2O_3 (Y_2O_3:Eu^{3+}), it was already observed that its luminescent properties are directly influenced by the morphology, particle size, crystalline structure and dopant concentration. Curiously, all these properties are mainly dependent on the synthesis method [3-9].

At room conditions, RE-SOs exhibit three polymorphic modifications depending on the cation radius: i) a cubic bixbyite-type phase, named C-type (S.G. $Ia\bar{3}$, No. 206, Z = 16), for small cations from Tb to Lu, including Y and Sc (Fig. 1(a)); ii) a monoclinic phase, named B-type (S.G. $C2/m$, No. 12, Z = 6), for medium-size cations from Sm to Gd (Fig. 1(c)); and iii) a trigonal phase, named A-type (space group (S.G) $P\bar{3}m1$, No. 164, Z = 1), for large cations from La to Nd (Fig. 1(b)). At room conditions, the most stable Y_2O_3 polymorph is the cubic C-type structure, but the metastable monoclinic B-type structure, is known to be obtained using different growth conditions: i) at high pressure (HP) and high temperature (HT) [10-15]; ii) under high-energy ion irradiation [16]; and iii) through a high-energy mechanical milling [17].

* Corresponding authors.
E-mail addresses: andreljp@ita.br (A.L.J. Pereira), fjmanjon@fis.upv.es (F.J. Manjón).

https://doi.org/10.1016/j.rinp.2023.106499
Received 3 February 2023; Received in revised form 18 April 2023; Accepted 26 April 2023
Available online 6 May 2023

As an industrial material, the knowledge of the structural stability of the Y_2O_3 polymorphs is important. In particular, a hexagonal phase (S.G. $P6_3/mmc$, No. 194, Z = 2) has been observed at HT [18] and both the monoclinic B-type phase and the trigonal A-type phase have been observed at HP [19]. In this context, a number of studies have investigated the HP properties of most RE-SOs both in bulk and nanocrystalline form. From those studies, recent reviews have concluded that the structural and vibrational properties of bulk RE-SOs are better known under compression than those of their nanocrystalline counterparts [20,21]. Regarding Y_2O_3, a number of HP works have studied bulk and nanocrystalline (pure and doped) Y_2O_3 under compression [10-12,22-48]. Notably, the published works show that the evolution of the Y_2O_3 properties at HP depend on the particular characteristics of the samples (bulk, nanoparticles, and nanotubes) and the compression conditions.

As regards bulk Y_2O_3, the structural, vibrational, and photoluminescent properties have been extensively studied at HP [10-14,19,22,24,25,29-33,36,37,41-44,47-49]. Some room-temperature HP studies have evidenced a C-B-A sequence of phase transitions (PTs) in bulk Y_2O_3 and Y_2O_3:Eu^{3+} on the upstroke [19,22,24,25,33,47,49]; while other works have claimed that only the C-A pressure-induced PT is observed in bulk Y_2O_3 [22,48]. In this scenario, several HP works have reported X-ray diffraction (XRD) and photoluminescence (PL) measurements in bulk Y_2O_3 and Y_2O_3:Eu^{3+} showing contradictory results regarding the pressure-induced PTs on the upstroke. Curiously, the only HP work reporting HP-Raman scattering (RS) measurements in bulk Y_2O_3 claimed the C-B-A PT sequence [19]. However, no comparison of the experimentally observed Raman frequencies and pressure coefficients with lattice-dynamics theoretical calculations was reported in that work to give support to the assignments of the different Raman-active modes of bulk Y_2O_3 in any of the different phases observed at HP. In this context, we want to stress that the comparison between experimental and theoretical results on vibrational properties at HP can help identify the different vibrational modes of the different HP phases and provide an alternative way to identify the Y_2O_3 polymorphs, as already proved in a number of compounds [50-53]. Additionally, experimental and theoretical results on Y_2O_3 under compression can complement the experimental studies already performed on bulk Y_2O_3 at room pressure [54-59], as well as the theoretical calculations on the properties of bulk Y_2O_3 that have been already reported [60-66]. In summary, there is a scarcity of HP-RS studies in bulk Y_2O_3, no HP-RS studies have been compared to theoretical calculations, there is no study on bulk Y_2O_3 comparing HP-XRD and HP-RS measurements on the same sample, and there is a controversy regarding the pressure-induced PT sequence on the upstroke; i.e. whether the intermediate B-type phase occurs or not.

In order to solve the still ongoing controversies on the behavior of bulk Y_2O_3 under compression and complement previous studies, we have performed a joint experimental and theoretical work in which HP-XRD and HP-RS measurements on the same sample of bulk Y_2O_3, the two most powerful techniques to identify phases at HP, have been contrasted to state-of-the-art theoretical *ab initio* calculations [53,63]. We will show that the results of the structural and vibrational properties of bulk Y_2O_3 confirm the C-B-A PT sequence on bulk Y_2O_3 on upstroke and the A-B PT sequence on downstroke. This result is in good agreement with what has been observed in RE-SOs of cations with similar ionic radius to Y, like Ho_2O_3 and Dy_2O_3, and ends with the controversy regarding whether the

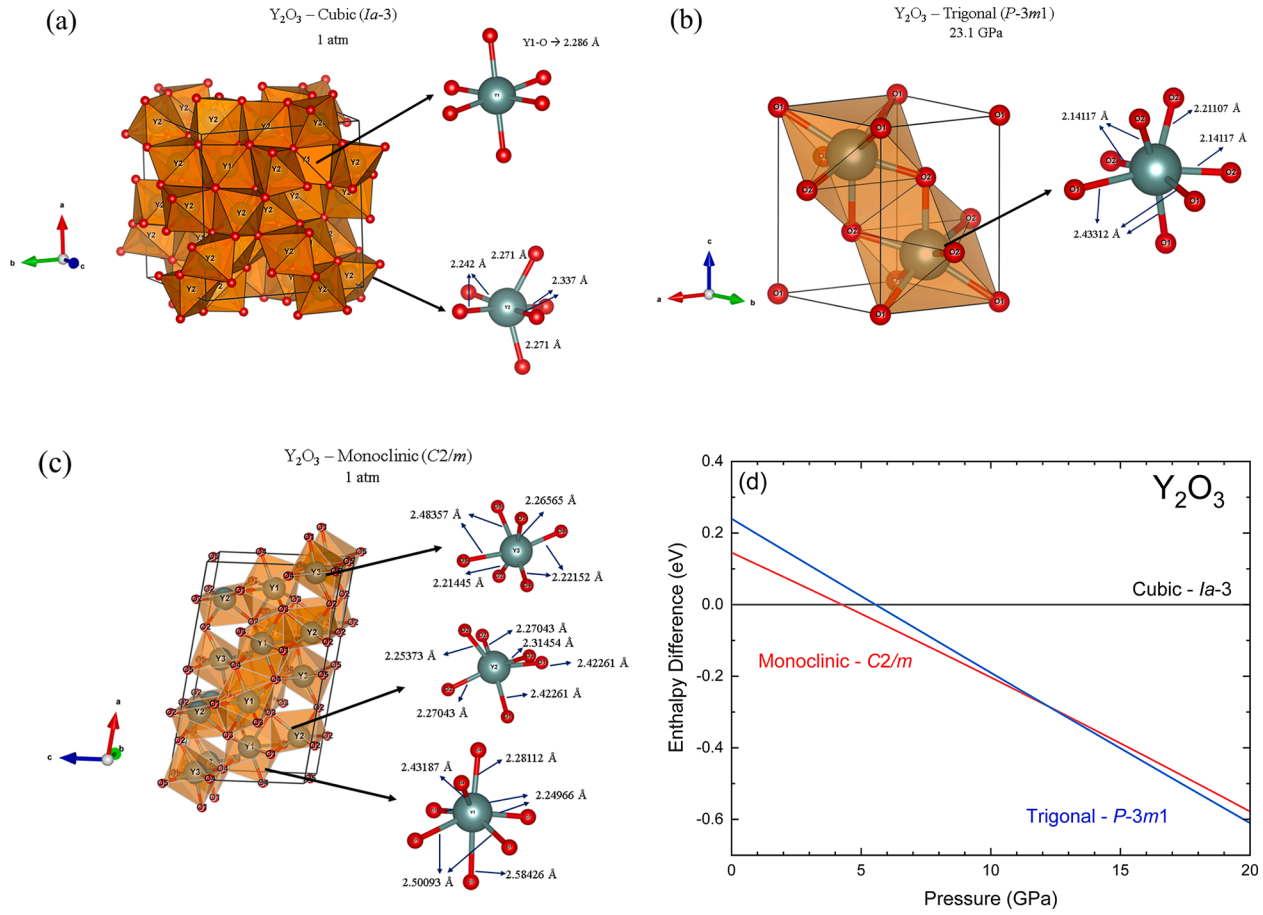

Fig. 1. Crystal structure and Y-O bond distance of the (a) cubic ($Ia\,\bar{3}$ SG 206, C-type), (b) trigonal ($P\,\bar{3}\,m1$, SG 164, A-type) and (c) monoclinic ($C12/m1$, SG 12, B-type) Y_2O_3. (d) Theoretical calculation of the enthalpy difference as a function of pressure for the cubic, trigonal, and monoclinic phases of Y_2O_3. Enthalpy of the cubic phase is taken as reference.

intermediate B-type structure is observed in bulk Y_2O_3 between the C- and A-type structures at HP. On the other hand, our HP-RS measurements provide a much better characterization of the vibrational properties of bulk Y_2O_3 under compression in the three observed phases than the only work reported to date [19]. Moreover, we provide theoretical *ab initio* calculations that are compared to our experimental measurements. We will show that the good agreement between experimental and calculated results for bulk Y_2O_3 has allowed us to provide: i) a detailed discussion of the structural behavior of the three phases under compression (unit-cell volumes, lattice parameters, free atomic parameters, Y-O bond distances, and polyhedral distortion indices); and ii) a detailed assignment of the symmetry of the Raman-active modes of the C-, B-, and A-type phases of Y_2O_3. In particular, we have confirmed the F_g nature of the most intense Raman-active mode in C-type Y_2O_3.

Experimental methods

Bulk Y_2O_3 samples studied in this work were commercial polycrystalline powders of Sigma-Aldrich with purity of 99.99% and with no additional treatment. Powder angle-dispersive HP-XRD measurements were performed at room temperature at the I15 beamline of DIAMOND Light Source and the BL04-MSPD beamline [67] of the ALBA synchrotron. In both cases a monochromatic X-ray beam with $\lambda = 0.4246$ Å was used. The sample was loaded with a 16:3:1 methanol-ethanol–water mixture as a pressure-transmitting medium (PTM) in a LeToulec-type diamond anvil cell (DAC) with diamond culets of 400 μm in diameter [68]. The pressure was determined by the equation of state (EoS) of copper [69]. Integration of 2D diffraction images was performed with Dioptas software [70] while structural analysis was performed by Le Bail refinements using FullProf [71] and PowderCell [72] program packages.

Unpolarized RS measurements were performed with the Horiba Jobin Yvon LabRAM HR UV microspectrometer equipped with a thermoelectrically cooled multichannel charge-coupled device detector and a 1200 grooves/mm grating that allows a spectral resolution better than 3 cm^{-1}. The signal was collected in backscattering geometry exciting with a 532 nm laser with a power of less than 10 mW. The sample was loaded with a 16:3:1 methanol-ethanol–water mixture in a membrane-type DAC and pressure was determined by the ruby luminescence method [73]. Phonons were analyzed by fitting Raman peaks with a Voigt profile fixing the Gaussian linewidth (2.4 cm^{-1}) to the experimental setup resolution. In all experiments, the DAC loading was performed taking care of avoiding sample bridging between the diamonds [74].

Simulations details

Ab initio total-energy calculations at 0 K for the C-, B-, and A-type phases of bulk Y_2O_3 have been performed within the Density Functional Theory (DFT) [75] framework with the Vienna Ab-initio Simulation Package (VASP) [76,77]. The pseudopotential method and the projector augmented waves (PAW) scheme [78,79] were employed with the plane-wave basis set extended up to an energy cutoff of 520 eV. This cutoff energy ensures a very good convergence of the energy difference and the isotropic pressure (Fig. S1 in the Supplementary Information (SI)). The generalized gradient approximation (GGA), with the Perdew-Burke-Ernzerhof parametrization extended for solids (PBEsol) [80], was used to describe the exchange and correlation energy. The Brillouin zones of these structures were sampled with dense Monkhorst − Pack meshes [81] of special *k*-points ($6 \times 6 \times 6$ for the C-type phase, $7 \times 7 \times 3$ for the B-type phase, and 6x6x6 for the A-type phase, using the primitive cell). This method ensures a high convergence of 1–2 meV per formula unit in the total energy and an accurate calculation of the forces on atoms. For each of the studied phases, the structures were fully relaxed to the optimized configuration, at sets of selected volumes, through the calculation of the forces on atoms and the stress tensor. The optimization criteria were to obtain forces on the atoms smaller than 0.005 eV/Å and deviations of the stress tensor from the diagonal hydrostatic form shortest than 0.1 GPa. The main structural parameters obtained by our theoretical calculations for the three phases of Y_2O_3 at selected pressures are given in the SI. Lattice-dynamical properties, frequency, and symmetry of the phonon modes were obtained at the Γ point of the Brillouin zone using the direct-force constant approach [82].

Results and discussion

Structural study of bulk Y_2O_3 under compression

In order to perform a structural analysis of bulk Y_2O_3 we carried out HP-XRD measurements up to 25.9 GPa (Fig. 2(a)). The two most intense peaks initially at ~ 11.8° and ~ 13.4° are related to the Cu intentionally placed in the pressure chamber to be used as a pressure sensor and were removed from Fig. 2 in order to facilitate the visualization of the Y_2O_3 peaks. Clearly, the Y_2O_3 peaks at low pressures correspond to C-type Y_2O_3 (see pattern of 0.4 GPa in Fig. S2 in the SI) and shift to higher angles and increase in linewidth as pressure increases. This result indicates a normal pressure-induced decrease of the interplanar distances in bulk C-type Y_2O_3. At 12.7 GPa, the intensity of the peaks corresponding to the cubic phase begins to decrease and, at 14.5 GPa, a new peak at ~ 8.7° unrelated to the initial phase (see orange arrow in Fig. 2 (a)) is detected. This peak is consistent with both the $(40\bar{2})$ and $(10\bar{1})$ peaks of the B- and A-type phases, respectively, since they are among the strongest peaks of both phases (see comparison of the simulated XRD patterns of the C-, B-, and A-phases near 18 GPa in Fig. S2). Moreover, another new peak can be detected at ~ 17.0 GPa below 8° (see orange arrow in Fig. 2(a)), thus confirming the PT to either the B- or A-type phase since this is the third of the four strongest peaks in both phases (see Fig. 2(b)). The above PT pressures and the phase coexistence of B and A phases is consistent with previous HP-XRD measurements in bulk Y_2O_3 [24,25]. We will see latter that the appearance of these two peaks near 14.5 and 17 GPa are also consistent with the onset of the C-B and B-A PTs above 13 and 16 GPa as proved by our HP-RS measurements and lattice-dynamics calculations.

On downstroke from 25.7 GPa (Fig. 2(b)), the peaks related to the A-type phase lose intensity and it is possible to observe new peaks that correspond to the B-type phase at 10.2 GPa. The intensity of these peaks increases as pressure decreases and the XRD pattern is clearly dominated by peaks of the B-type phase at the lowest pressure. Note that the main peak of the A-type phase near 9° loses intensity and transforms into a peak of the B-type phase with similar intensity to the two peaks at lower angles. It is difficult to clearly assign the pressure at which the B-A transition occurs since many peaks observed above 12.7 GPa are common to both the B- and A-type phases and overlap with those of the C-type phase persisting up to 22.9 GPa. Also regarding this observation, it must be noted that the similarity of the XRD patterns of the B- and A-type phases could have been the reason to consider that only the C-A PT is observed in bulk Y_2O_3 in prior works [22,48]. We will show latter that these results in bulk Y_2O_3 on downstroke are compatible with our HP-RS results and evidence a mixture of phases above 12.7 GPa. It must be stressed that the C-B-A PT sequence in bulk Y_2O_3 here suggested on the upstroke is in agreement with what has been found in RE-SOs with cations of similar ionic radius as Y, such as Ho_2O_3 and Dy_2O_3 [83,84].

Once commented the sequence of pressure-induced PTs in bulk Y_2O_3 from the structural point of view, let us analyze the results of the structural properties of the different phases of Y_2O_3 at HP. For that purpose, we have performed a Le Bail refinement of the C-type phase from the XRD patterns presented up to 20.3 GPa in Fig. 2(a). Le Bail refinements performed at 0.4 GPa yield residuals of $R_p = 0.8\%$ and $R_{wp} = 1.4$ %, while those performed at 20.3 GPa yielded $R_p = 0.6\%$ and $R_{wp} = 1.3\%$. Unfortunately, the B-type and A-type phases are minority between 13.4 GPa and 20.3 GPa and have poorly defined peaks, so we have only performed refinements of the cubic phase in this pressure range.

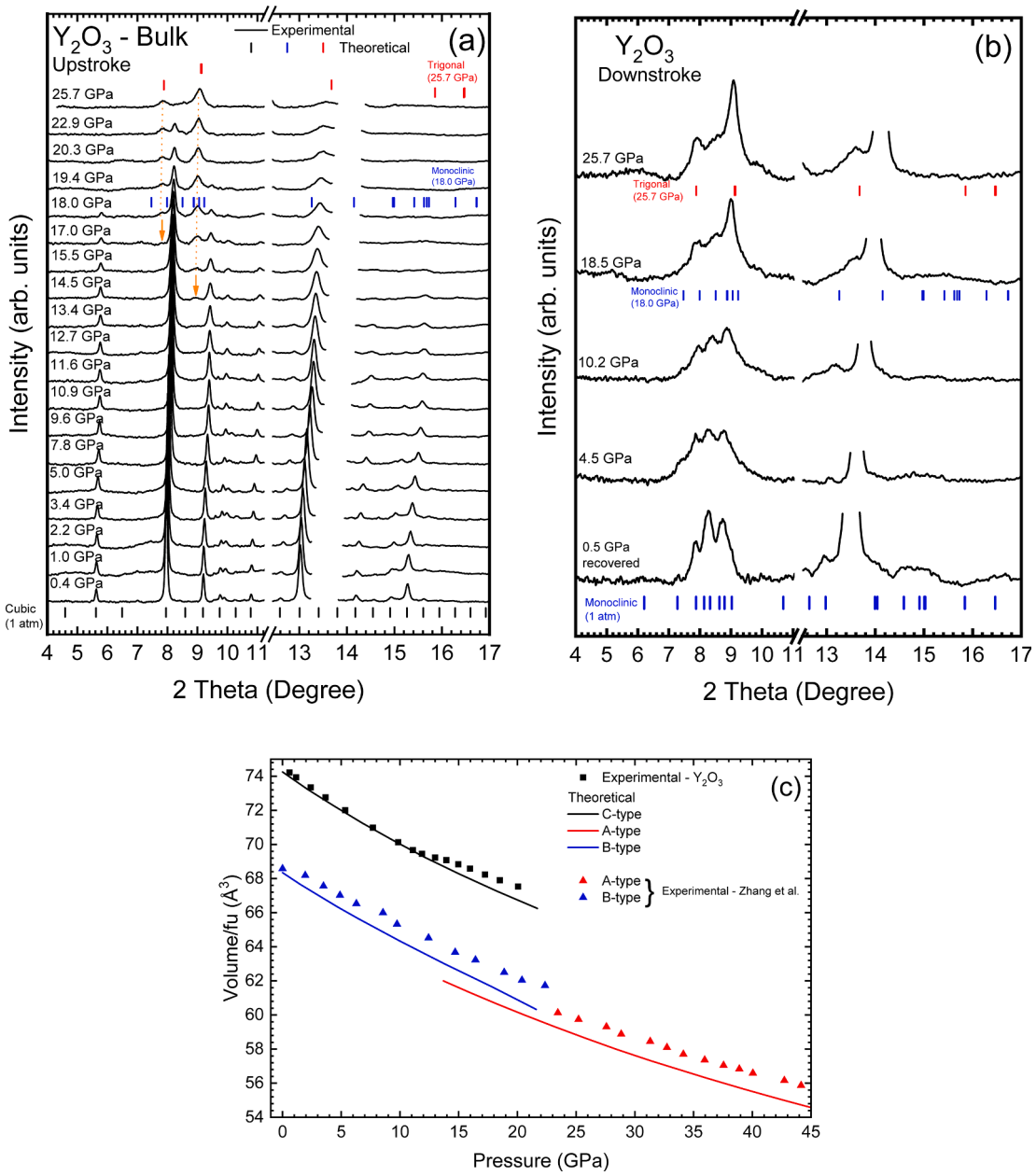

Fig. 2. Room-temperature XRD patterns of bulk Y_2O_3 at selected pressures on (a) upstroke and (b) downstroke. The orange arrows presented in (a) show the new peaks that appear with the pressure increase and that can be related to both monoclinic (B) and trigonal (A) phases. The empty spaces in (a) and (b) correspond to the metallic Cu peaks that were used as a pressure sensor and were removed in order to improve the visualization of the Y_2O_3 peaks. Black, red and blue vertical bars in figure (a) and (b) are the position of the diffraction peaks of the C-, A- and B-type phases, respectively, according to the data obtained from our theoretical calculations. Pressure dependence of the experimental (symbols) and theoretical (lines) unit-cell volume per formula unit (c) of the cubic phase on the upstroke. In figure (c), the experimental data obtained by Zhang et al. [41] for B- (blue) and A-type (red) phases are included for comparison with our theoretical values. Error bars of figures (c) are smaller than the symbol size of each experimental point. (For interpretation of the references to color in this figure legend, the reader is referred to the web version of this article.)

Unfortunately, above 20.3 GPa and on downstroke, the XRD patterns did not show enough resolution to perform a reliable refinement. Fig. 2(c) shows the experimental and theoretical pressure dependence of the unit-cell volume per formula unit (V/fu) of the cubic phase. As can be observed, there is a good correlation between the theoretical and experimental lattice parameters up to ~ 12 GPa. Above this pressure, the experimental results present an unexpected behavior, which may be related to the loss of PTM hydrostaticity, but also to the presence of other phases mixed with the cubic one, as already commented. In this context, the use of PTM in non-hydrostatic regimes can directly influence the determination of values of the bulk modulus (B_0) by the production of different deviatoric stresses that directly affect the pressure dependence of the unit-cell volume (V) [85-87]. This basically occurs because, if deviatoric components are present in the Cauchy stress tensor, the sample at HP may suffer both a compression (due to hydrostatic pressure) and an expansion caused by the Poisson effect (due to shear stresses), leading to an effective experimental compression that is smaller than that observed when only hydrostatic pressure is present [88].

Although we could not determine the experimental structural parameters of the B- and A-type phases of Y_2O_3 by Le Bail refinement, we have plotted the pressure dependence of the theoretical unit-cell

volumes per formula unit (Fig. 2(c)) and of the lattice parameters (Fig. S3 in the SI) for these two phases in order to compare them with data obtained from HP-XRD measurements in B-type Y_2O_3 [41]. As can be observed, our theoretical values of the unit-cell volumes for B- and A-type Y_2O_3 present a good agreement with the reported experimental data [41], thus reinforcing the good quality of our theoretical calculations. It is interesting to note that the theoretical *a* and *b* lattice parameters of the B-type phase (see Fig. S3(b)) show abrupt changes above ~ 12 GPa due to the difficulties found in simulating this phase above this pressure. Consequently, we only give credit to our theoretical calculations of the monoclinic B-type phase between 0 and 12 GPa. We will comment latter on these simulation difficulties when analyzing the vibrational properties of the monoclinic phase. In this context, we must mention that calculations of the trigonal A phase are completely trustworthy in the whole pressure range studied.

In order to obtain the experimental zero-pressure volume (V_0), bulk modulus (B_0), and its pressure derivative (B_0') for the cubic phase of bulk Y_2O_3, we performed a fit of our P-V data with a 3rd-order BM-EoS (Fig. 2 (c)) in the quasi-hydrostatic pressure range of the PTM (up to 12 GPa). On the other hand, for the theoretical P-V data of the cubic, trigonal, and monoclinic phases of bulk Y_2O_3, we performed a fit with a 3rd-order BM-EoS in the pressure ranges where these phases are stable. The experimental and theoretical results are summarized in Table 1. Our experimental 3rd-order BM-EoS fit for cubic bulk Y_2O_3 results in: V_0/fu = 74.517(8) Å^3, B_0 = 147(1) GPa and $B_0' = 3.2(3)$. These values agree well with our theoretical calculations for this phase (V_0/fu = 74.24(1) Å^3, B_0 = 154(1) GPa and $B_0' = 3.5(2)$) and are comparable with the results presented in previous experimental (135.7–149.5 GPa) [24,48,89-91] and theoretical (138–173 GPa) [24,29,63-66] studies for cubic bulk Y_2O_3. In this context, it must be stressed that our B_0 value in bulk Y_2O_3 is only slightly smaller than what is expected for RE-SOs of the same cation size as Y (~155–160 GPa) according to a recent review [21]. On the contrary, a much higher value of B_0 (180 GPa) was measured in cubic bulk Y_2O_3 when non-hydrostatic PTM, like silicon oil, was used [49]. Therefore, the present results show that our values for cubic bulk Y_2O_3 are consistent with what is expected for quasi-hydrostatic conditions. Additionally, the axial compressibility, κ_a, obtained from a modified BM-EoS fit [92] of the experimental and theoretical data in the quasi-hydrostatic pressure range of the PTM, is also reported in Table 1. Once again, there is a good agreement between the experimental and theoretical axial relative compressibilities at room pressure that are 2.3(5)0.10^{-3} GPa^{-1} and 2.18(8)0.10^{-3} GPa^{-1}, respectively.

The good agreement between our experimental and theoretical results on both structural and vibrational (we will see later) properties allows us to exploit our theoretical structural data to compare with experimental structural data already reported in the literature as in the case of B- and A-type Y_2O_3. In Fig. 2(c), we present the theoretical P-V data for the trigonal and monoclinic phases of bulk Y_2O_3 in the range where these structures are stable. As observed, our theoretical data are in very good agreement with reported experimental data [41]. As can be observed, a theoretical decrease of ~ 9 % (11%) in the V_0/fu at the C-B (C-A) PT is predicted at around 18 GPa; thus, confirming that they are first-order PTs. This result is consistent with the increase of ~ 2% in the volume of the unit cell at the A-B PT on downstroke at ~ 18 GPa. Moreover, this result is also compatible with results already published for bulk Y_2O_3 [49] and other RE-SOs [21,24,63,93,94], and suggests a weak first-order character of the A-B PT. The theoretical V_0, B_0, and B_0' values of the A- and B-type phases of bulk Y_2O_3, obtained after a fit the theoretical P-V curves with a 3rd-order BM-EoS, are summarized in Table 1. The values obtained are in good agreement with experimental [24,41,48] and theoretical [48,63] values already reported, reinforcing the validity of our theoretical calculations in the study of the different phases of Y_2O_3 at HP. In this context, the comparison of our theoretical values with experimental ones allows us conclude once again that much larger values for the bulk moduli of A- and B-type phases were obtained when a non-hydrostatic PTM was used as in Ref. [49].

Through our theoretical calculations, we were able to estimate the axial compressibility of both A- (κ_a and κ_c) and B-type (κ_a, κ_b, κ_c) phases

Table 1

EOS parameters and axial compressibility ($\boldsymbol{\kappa_a} = \frac{-1}{\boldsymbol{a}}\frac{\partial \boldsymbol{a}}{\partial \boldsymbol{P}}$) at room pressure of the experimental cubic phase of bulk Y_2O_3 as well as of the theoretical cubic, trigonal, and monoclinic phases of bulk Y_2O_3. The variation $\frac{\partial \boldsymbol{a}}{\partial \boldsymbol{P}}$ was obtained using the modified Murnaghan equation of state $\Delta \boldsymbol{a}_0/\boldsymbol{a}_0 = \left(1 + \boldsymbol{K}_0'\boldsymbol{P}/\boldsymbol{K}_{I0}\right)^{-\left(\frac{1}{3\boldsymbol{K}_0'}\right)} - 1$, were $\boldsymbol{K}_{I0}$ and $\boldsymbol{K}_0'$ are the bulk modulus and its pressure derivative for the *a*-axis at room pressure. In order to simplify the comparation between the structures, V_0 is presented per formula unit (fu): cubic (Z = 16); trigonal (Z = 1); monoclinic (Z = 6). Our values are compared to other values found for bulk and nanocrystalline samples in the literature.

	V_0/fu (Å^3)	B_0 (GPa)	B_0'	κ_a (10^{-3} GPa^{-1})	κ_b (10^{-3} GPa^{-1})	κ_c (10^{-3} GPa^{-1})
Experimental						
C-type bulk *	74.517(8)	147(1)	3.2(3)	2.3(5)	–	–
	74.49(7)[a], 74.633(3)[b]	147(2)[a], 180(3)[b]	4(fixed)[a,b]	–	–	–
C-type Nanotubes	75.0(2)[c], 74.6(1)[d]	145(5)[c],134(20)[d]	4(fixed)[c], 5.6(3.9)[d]	–	–	–
A-type bulk	66.78(53)[a],67.79[e],67.9(2)[b]	159(15)[a], 156(3)[e], 177(7)[b]	4(Fixed)[a,e,b]	–	–	–
B-type bulk	68.55(12)[a], 68.99(10)[e], 71.42[f]	155(4)[a], 159(3)[e], 192(10)[f]	4(fixed)[a,e,f]	–	–	–
Theoretical (bulk material)						
C-type Y_2O_3						
This work (GGA-PBEsol)	74.24(1)	154(1)	3.5(2)	2.18(8)	–	–
LDA [a]	71.58	163.5	3.98	–	–	–
GGA – PBE [g]	74.312	165.2	5.0	–	–	–
A-type Y_2O_3						
This work (GGA-PBEsol)	66.95(5)	157(2)	3.24(8)	1.1(7)	–	13(2)
PAW [h]	69.58	136	3.5(fixed)	–	–	–
LDA[a]	64.63	144.6	4.37	–	–	–
B-type Y_2O_3						
This work (GGA-PBEsol)	68.342(8)	151(1)	3.0(2)	3.9(2)	1.3(2)	2.1(3)
PAW [h]	70.78	138	3.5(fixed)	–	–	–
LDA[a]	66.16	117.9	4.83	–	–	–

* Our values correspond to fits up to 12 GPa, [a] Ref. [24], [b] Ref. [49] [c] Ref. [34], [d] Ref. [26], [e] Ref. [41], [f] Ref. [25], [g] Ref. [65], [h] Ref. [95], [i] Ref. [48].

of Y_2O_3. As can be observed in Table 1, the *c*-axis of the trigonal phase has a relatively higher axial compressibility than the *a*-axis. This result was already observed and was attributed to the largest empty spaces between the layers oriented in the *c*-axis direction [41]. With respect to the monoclinic phase, we observed rather different axial pressure coefficients, being that of the *a*-axis (highest pressure coefficient) three times higher than that of the *b*-axis (lowest pressure coefficient). The highly anisotropic behavior found for A- and B-type phases of Y_2O_3 is in agreement with that previously found in Y_2O_3 [41] and in other RE-SOs, such as Ho_2O_3 [83] and Dy_2O_3 [84], with similar unit cell volumes since Y, Ho, and Dy have similar ionic radii.

At this point, it is important to comment that the values for the axial compressibilities in monoclinic and triclinic structures are not significant since the three lattice parameters are not orthogonal (angles different from 90°). In order to have significant results on B-type Y_2O_3, we have to obtain the directions of maximum and minimum compressibility by diagonalising the theoretical isothermal compressibility tensor, β_{ij} [96]. The tensor coefficients for a monoclinic crystal with *b* as the unique crystallographic axis are given by [97]:

$$\beta_{ij} = \begin{pmatrix} \beta_{11} & 0 & \beta_{13} \\ 0 & \beta_{22} & 0 \\ \beta_{13} & 0 & \beta_{33} \end{pmatrix}$$

The theoretical isothermal compressibility tensor coefficients for monoclinic Y_2O_3 at 0 GPa have been calculated using the IRE (Institute of Radio Engineers) convention for the orthonormal basis for the tensor: $e_3||c$, $e_2||b^*$, $e_1||e_{2\times}e_3$. The tensor has been obtained with the finite Eulerian approximation as implemented in the Win_Strain package [98].

The theoretical elements of this tensor at 0 GPa are reported in Table 2 in which the values of the maximum, intermediate, and minimum compressibility and their corresponding directions are given by the eigenvalues (λ_i, i = 1–3) and eigenvectors (ev_i, i = 1–3), respectively.

The calculated axial compressibilities (β_{ii} coefficients) at 0 GPa fulfill that $\beta_{11} > \beta_{33} > \beta_{22}$. This result shows that the compressibility along the *a*-axis is greater than those to the *c*-axis and *b*-axis. A diagonalization of the β_{ij} tensor at 0 GPa yields for our calculations the maximum, intermediate and minimum compressibilities $3.5(4)\cdot10^{-3}$, $1.7(4)\cdot10^{-3}$ and $1.6(3)\cdot10^{-3}$ GPa^{-1}, respectively. These theoretical results indicate that around 52% of the total compression at 0 GPa occurs in the direction of maximum compressibility. Considering the eigenvector ev_1, the major compression direction at 0 GPa occurs in the (0 1 0) plane at the given angle Ψ (see Table 2) relative to the *c*-axis (from *c* to *a*) or equivalently at an angle θ relative to the *a*-axis (from *a* to *c*). In particular, the major compression direction is at θ = -19(3)° from the *a*-axis. The theoretical direction of intermediate compressibility, given by eigenvector ev_2, is in the (0 1 0) plane perpendicular to the direction of maximum compressibility, and the direction of minimum compressibility, given by eigenvector ev_3, is along the *b* axis.

Table 2
Theoretical isothermal compressibility tensor coefficients, β_{ij}, and their eigenvalues, λ_i, and eigenvectors, ev_i, for Y_2O_3 at 0 GPa. The results are given using the finite Eulerian method. The eigenvalues are given in decreasing value along the column.

β_{11} (10^{-3} GPa^{-1})	3.1(3)
β_{22} (10^{-3} GPa^{-1})	1.6(4)
β_{33} (10^{-3} GPa^{-1})	2.1(3)
β_{13} (10^{-3} GPa^{-1})	−0.75(9)
λ_1 (10^{-3} GPa^{-1})	3.5(4)
ev_1 (λ_1)	(-0.88,0,0.48)
λ_2 (10^{-3} GPa^{-1})	1.7(4)
ev_2 (λ_2)	(0.48,0,0.88)
λ_3 (10^{-3} GPa^{-1})	1.6(3)
ev_3 (λ_3)	(0,1,0)
Ψ, θ (°)[a]	119(3), −19(3)

[a] The major compression direction occurs in the (0 1 0) plane at the given angle Ψ to the *c*-axis (from *c* to *a*) and θ to the *a*-axis (from *a* to *c*).

Let us now discuss about the pressure dependence of Y-O bond distances and polyhedral distortion in the different phases of bulk Y_2O_3. As previously stated, the cubic Y_2O_3 unit cell is composed of two types of Y^{3+} atoms (Y1 and Y2), each surrounded by six oxygen atoms (O1). While O atoms around Y1 form a regular octahedron, O atoms around Y2 atoms form a distorted octahedron. To our knowledge, very few experimental information and no theoretical information has been published regarding the pressure dependence of the Y-O bond distances in the cubic phase of Y_2O_3. In Fig. S4(a) and S4(b) in the SI, we present the theoretical pressure dependence of the Y-O bond distances and the distortion index of the Y2 octahedron, respectively, as obtained from the VESTA software [99]. As observed, all bond distances present a monotonous decrease upon compression, so there is no net increase of the Y coordination number in the cubic phase at HP. Performing a simple linear fit, we observe that the three shortest distances present a decrease rate of $\sim 4.0\cdot10^{-3}$ Å/GPa, while the largest Y2-O1 distance decrease at $2.7\cdot10^{-3}$ Å/GPa. This behavior is directly related to the decrease of the unit-cell volume and the increase of the Y2 octahedral distortion index of $3.3(1)\cdot10^{-4}$ GPa^{-1} (see Fig. S4(b)), while the Y1 octahedron does not present any distortion. For comparison, we have added the experimental results presented by Li *et al.* [34] for cubic bulk Y_2O_3:Eu^{3+} nanotubes in Fig. S4(a). As can be observed, there is a good agreement between our theoretical results and the experimental ones presented by Li *et al.* up to ~ 4 GPa (see Fig. S4(b)). Above this pressure, the experimental Y2-O1 distances present a non-monotonous behavior and cannot be compared to our theoretical results. Unfortunately, we cannot comment on the cause for the anomalous behavior of the experimental parameters reported by Li *et al.*, but since the anomalous behavior is found above 8 GPa it can be speculated that non-hydrostatic effects and/or the mixture with the first HP phase in Ref. 34 could be the cause for the disagreement between experiment and theory, as it occurs with our own HP-XRD measurements.

Regarding the A-type phase of Y_2O_3, it is composed of only one type of Y atoms and two types of O atoms, being the Y atom surrounded by seven O atoms in a distorted polyhedron (Fig. 1(b)). In Fig. S5(a) and S5 (b) in the SI, we present the theoretical pressure dependence of the Y-O bond distances and the distortion index of the polyhedron around the Y atom, respectively, in A-type Y_2O_3. To our knowledge, there are no reported experimental data of Y-O bond distances in A-type Y_2O_3 to compare with. As can be observed in Fig. S5(a), the Y1-O2 bond distances in A-type Y_2O_3 remain at values comparable with the Y-O bond distances in C-type Y_2O_3; however, the Y1-O1 distance in A-type Y_2O_3, present a significant increase in the bond distance compared with the Y-O bond distances in C-type Y_2O_3. This abrupt change in the bond distances upon the C-A PT is consistent with the unit-cell volume discontinuity observed in Fig. 2(c) and allows attaining the sevenfold coordination to Y atoms in the A-type structure. Performing a simple linear fit, we obtain that the Y1-O1 distance in A-type Y_2O_3 decrease rate of 4.3 10^{-3} Å/GPa, while the two Y1-O2 distances decrease at a rate of $3.6\cdot10^{-3}$ Å/GPa (largest distance) and $1.8\cdot10^{-3}$ Å/GPa (shortest distance). The decrease in the bond distances with pressure in A-type Y_2O_3 is accompanied by a decrease in the distortion index ($\sim3.5\cdot10^{-4}$ GPa^{-1}) of the YO_7 polyhedron (Fig. S5(b)).

Regarding the B-type phase of Y_2O_3, it is composed of three different types of Y and O atoms, being Y1 surrounded by seven O atoms and Y2 and Y3 surrounded by six O atoms (Fig. 1(c)). This configuration results in thirteen different Y-O bond distances in the unit cell. As can be seen in Fig. S6(a) in the SI, some theoretical bond distances of the B-type phase appear to be a continuation of the bond distances of the A-type phase. Again, to our knowledge, there are no reported experimental data of Y-O bond distances in B-type Y_2O_3 to compare with. The relatively smooth change in bond distances (all ranging between 2.15 and 2.55 Å) may be responsible for the smaller unit-cell volume variation observed in Fig. 2 (c) characteristic of the B-A PT, which is an “almost” displacive PT. It is

interesting to note in Fig. S6(a) that, while most Y-O distances in B-type Y_2O_3 decrease at HP, some distances show the opposite trend above 10 GPa, thus suggesting an anomalous behavior of the simulations of this phase at higher pressures, as already commented. Regarding the distortion index of the different polyhedra in B-type Y_2O_3, the polyhedra of Y1 and Y2 atoms initially have a decreasing trend up to ~ 5 GPa and ~ 8 GPa, respectively, and an increasing trend above those pressures (see Fig. S6(b)). On the other hand, the distortion index of the Y3 polyhedron has the highest value of the three polyhedra at room pressure and tends to increase at HP.

To finish the discussion regarding the structural features of bulk Y_2O_3 at HP, we show in Fig. S7 and Fig. S8 in the SI the theoretical pressure evolution of the free atomic parameters in C-type and A-type Y_2O_3, respectively. In C-type Y_2O_3, the x position of the Y2 and O1 atoms show a slight decrease (0.1 and 0.3%) between 0 and 15 GPa. On the other hand, O1(y) and O1(z) show a similar increase (0.1 and 0.2%) in the same pressure range (Fig. S7). These very small variations indicate that the monotonous decrease in bonding distances of the cubic phase is mainly related to the decrease in unit-cell volume and not to the variation of atomic positions; a result in good agreement with what has been recently published in Tb_2O_3 [21]. Similarly, the Y1(z) (O2(z)) position of A-type Y_2O_3 (Fig. S8) show a decrease (increase) of 2% (0.5%) between 15 (30) GPa. This means that there are also rather small variations of the atomic parameters in this phase and that the monotonous decrease in bonding distances of the A-type phase is mainly related to the decrease in unit-cell volume and not to the variation of atomic positions. This result is again in good agreement with what has been recently discussed for the A-type phase of Tb_2O_3 [21]. The same seems to occur in the B-type phase of RE-SOs as recently discussed [21].

In summary, HP-XRD measurements and *ab initio* calculations on bulk Y_2O_3 suggest that this compound undergoes a PT from the C-type phase either to the B- or A-type phase and ultimately to the A-type phase on increasing pressure and an A-B PT on decreasing pressure, being the B-type phase metastable at room conditions. This result is consistent with previous results on RE ions of similar size to Y. We will show in the next section that these results agree with ours and previous HP-RS measurements in bulk Y_2O_3 that confirm the C-B-A PT sequence on upstroke and disagree with some previous HP-XRD measurements in bulk Y_2O_3 that interpreted that the B-type phase was not observed on the upstroke. As we have shown, the discrepancy with previous HP-XRD measurements in bulk Y_2O_3 is due to the difficulty in differentiating between the diffraction peaks of the B and A-type phases, featuring a group-subgroup relationship. This differentiation is even more difficult when these two phases coexist with the original C-type phase on upstroke. In this context, the comparison of experimental results with theoretical results from *ab initio* calculations is important to resolve the ongoing controversy. On the other hand, our calculations show good agreement with our and previous HP-XRD measurements and evidence that the evolution of the lattice parameters, interatomic distances, and atomic parameters of the three phases of bulk Y_2O_3 at HP, previously not reported for all phases, is similar to those of the recently published three phases of bulk Tb_2O_3 [21]. This means that we can conclude that we have disclosed the general behavior of RE-SOs under compression.

Vibrational study of bulk Y_2O_3 under compression

Now we will perform a vibrational study of bulk Y_2O_3 at HP by means of experimental HP-RS measurements compared to theoretical lattice-dynamics calculations. For this purpose, we must consider the Raman-active modes expected for each of the different structures we can find. As regards cubic C-type Y_2O_3, its unit cell contains three independent atoms: two inequivalent Y atoms, located at 8*b* (Y1) and at 24*d* (Y2) Wyckoff sites, and one O atom located at a 48*e* site. Therefore, there are 120 normal modes of vibration at the zone center of the Brillouin zone of cubic Y_2O_3, whose mechanical representation is:

$$\Gamma_{\text{cubic}} = 4A_g(R) + 4E_g(R) + 14F_g(R) + 5A_u(I) + 5E_u(I) + 16F_u(IR) + 1F_u(Ac)$$

where A_g, E_g and F_g (or T_g) modes are Raman-active (R), A_u and E_u modes are inactive (I), and all F_u modes are infrared-active (IR) except one F_u mode that corresponds to the three acoustic (Ac) modes. Note that the E modes are doubly degenerated, and the F modes are triply degenerated. Thus, 22 Raman-active modes ($\Gamma_{Raman} = 4A_g + 4E_g + 14F_g$) are expected, being 15 modes ($3A_g + 3E_g + 9F_g$) related to the vibrations of O atoms at 48*e* sites and seven modes ($A_g + E_g + 5F_g$) related to the vibrations of Y^{3+} atoms at 24*d* sites.

On the other hand, the unit-cell of monoclinic B-type Y_2O_3 contains eight independent atoms: three Y atoms located at 4*i* Wyckoff sites and five O atoms, four of them located at 4*i* Wyckoff sites and one located at a 2*b* site. Therefore, there are 45 normal modes of vibration at the zone center of the Brillouin zone of monoclinic Y_2O_3, whose mechanical decomposition is:

$$\Gamma_{monoclinic} = 14A_g(R) + 7B_g(R) + 7A_u(IR) + 14B_u(IR) + A_u(Ac) + 2B_u(Ac)$$

thus, 21 Raman-active modes ($\Gamma_{Raman} = 14A_g + 7B_g$) and 21 IR-active modes ($\Gamma_{IR} = 14A_u + 7B_u$) are expected.

Finally, the unit-cell of trigonal A-type Y_2O_3 contains three independent atoms: one Y atom located in a *2d* Wyckoff position and two O atoms located in *1a* and *2d* Wyckoff positions. Therefore, there are 15 normal modes of vibration at the zone center of the Brillouin zone of trigonal Y_2O_3, whose mechanical decomposition is:

$$\Gamma_{trigonal} = 2A_{1g}(R) + 2E_g(R) + 2A_{2u}(IR) + 2E_u(IR) + A_{2u}(Ac) + E_u(Ac)$$

thus, four Raman-active modes ($\Gamma_{Raman} = 2A_g + 2E_g$) and four IR-active modes ($\Gamma_{IR} = 2A_{2u} + 2E_u$) are expected. Note that E modes are doubly degenerated.

Fig. 3(a) shows the RS spectra of pure bulk cubic Y_2O_3 at selected pressures up to 30 GPa. It can be observed that up to nine modes could be followed under pressure. All peaks tend to shift to higher frequencies at HP, except the peak initially at 129.7 cm^{-1} that has a negative pressure coefficient. Moreover, an additional weak peak at ~ 410 cm^{-1} at 6.1 GPa, that initially was overlapped by the most intense peak initially at 377.2 cm^{-1}, was observed. Therefore, our HP-RS measurements are consistent with those previously reported for bulk cubic Y_2O_3 [19], and are extended to higher pressures than in the previous work.

Up to 13.2 GPa, RS spectra only show peaks of the cubic phase, but above 14.7 GPa new bands (around 160, 500 and 550 cm^{-1}) and a broad band with several peaks (between 250 and 400 cm^{-1}) appear, that show the onset of a PT in coexistence with the peaks of the cubic phase. Finally, above 17.9 GPa, a new broad band appears around 470 cm^{-1} (overlapping with the weak mode of the cubic phase mentioned in the previous paragraph). Concomitantly, the peaks of the cubic phase show a strong decrease in intensity and the strongest one disappears above 20.4 GPa. We will later discuss that these new peaks appearing above 14.7 GPa correspond to the monoclinic B-type phase.

Above 25 GPa, almost all modes of the monoclinic phase disappear, and it is possible to observe four peaks that are coincident with some of the monoclinic phase at ~ 170, 300, 540 and 580 cm^{-1} at 25.6 GPa. This result confirms the completion of the B-A PT above this pressure, belonging all modes above this pressure to the A phase. In this context, it must be noted that the RS spectrum of the A-type phase at 29.5 GPa also shows three broad bands around 250, 400 and 700 cm^{-1}. We consider that they likely correspond to second-order Raman modes of the A phase that we tentatively attribute to A^2_{1g}-A^1_{1g}, E^2_g-E^1_g and $E^1_g + A^2_{1g}$, respectively. In conclusion, our HP-RS measurements show a pressure-induced C-B-A PT sequence in bulk Y_2O_3 on upstroke that agrees with our HP-XRD measurements. This PT sequence also agrees with that observed in the only published HP-RS measurements on bulk Y_2O_3 that observed the onset of the C-B and B-A PTs near 12 and 19 GPa, respectively [19].

On downstroke from 30 GPa (Fig. 3(b)), there are changes in the RS

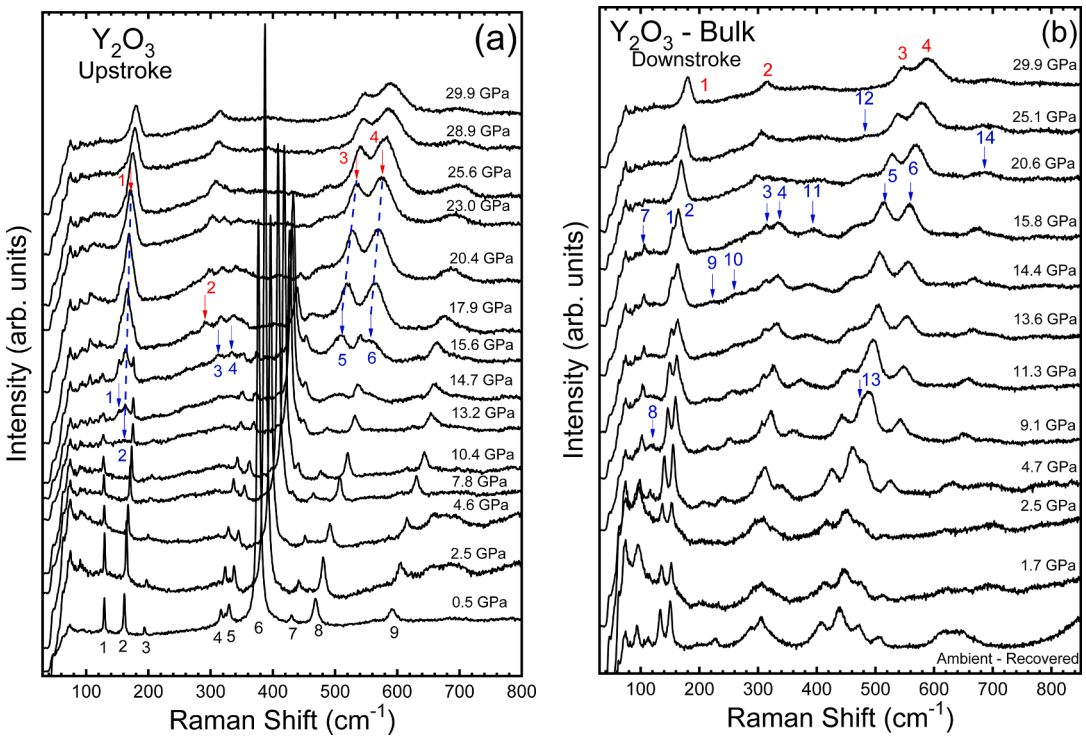

Fig. 3. Room-temperature Raman spectra of bulk Y_2O_3 at selected pressures on upstroke (a) and downstroke (b). Black numbers indicate initial peaks of cubic phase of bulk Y_2O_3, while blue and red arrows and numbers indicate the new peaks related to monoclinic and trigonal phases of bulk Y_2O_3, respectively. Note that the peaks marked with dashed blue lines on upstroke belong to the monoclinic phase and are the only ones that remain in the trigonal phase. (For interpretation of the references to color in this figure legend, the reader is referred to the web version of this article.)

spectrum of the trigonal phase around 300 cm^{-1} at 20.6 GPa. The changes are more evident at 15.8 GPa and at shortest pressures with the appearance of several peaks. Finally, the RS spectrum of the recovered sample at 1 atm seems to retain the same structure observed at 15.8 GPa. This structure is consistent with our HP-XRD measurements and with the monoclinic B-type phase observed in the recovered samples of all compressed C-type RE-SOs that undergo a PT to the B-type or A-type structure. Again, our observation of the recovery of the B-type phase on downstroke in bulk Y_2O_3 and the hysteresis of the B-A PT agrees with those reported for bulk Y_2O_3 in a previous HP-RS work [19].

In order to aid in the identification of the monoclinic polymorph of Y_2O_3 near room pressure conditions, we show the RS spectrum of B-type Y_2O_3 at room pressure on decreasing pressure in Fig. S9 in the SI. This phase was already identified by XRD and PL measurements at room pressure [41,100]. To our knowledge, only one RS spectrum of this phase at room conditions has been published [14], whose reported frequency range is smaller than ours. We want to stress that our RS spectrum of B-type Y_2O_3 is similar to that already reported [14] and to those of recently reported B-type Tb_2O_3 [21], Tm_2O_3 [101], and Gd_2O_3 [102]. The tentative assignment of the Raman-active modes of B-type Y_2O_3 will be latter discussed on the light of a close comparison between the experimental and theoretical Raman-active frequencies and their pressure coefficients.

Let us now discuss the effect of pressure on the vibrational properties of bulk Y_2O_3. Fig. 4 shows the pressure dependence of the experimental Raman-active frequencies of the C-, B-, and A-type phases in bulk Y_2O_3 compared to the theoretical ones on the upstroke (Fig. 4a and b) and the downstroke (Fig. 4c and d). As observed, there is a good agreement between the theoretical and experimental frequencies and pressure coefficients for the three phases up to 30 GPa, thus confirming the C-B-A PT sequence on the upstroke and the A-B PT on the downstroke in bulk Y_2O_3, as previously reported [19,22,24,25,33,47,49].

We can observe that the pressure dependence of the Raman-active frequencies of C-type Y_2O_3 (in Fig. 4a) is similar to those reported for other C-type RE-SOs, like Tb_2O_3 [21], Lu_2O_3 [103,104], Yb_2O_3 [105], Tm_2O_3 [101], Sc_2O_3 [106], and In_2O_3 [107], as recently reviewed [21]. Similarly, the pressure behavior of the Raman-active frequencies of B-type Y_2O_3 is similar to those reported for other B-type RE-SOs, including Tb_2O_3 [21], Lu_2O_3 [103,104], Yb_2O_3 [105], Tm_2O_3 [101], and Sm_2O_3 [108,109]. Finally, the pressure dependence of the Raman-active frequencies of A-type Y_2O_3 is also similar to those reported for A-type RE-SOs, like Tb_2O_3 [21], Sm_2O_3 [108,109] and Nd_2O_3 [110]. Therefore, the results of our HP-RS measurements on Y_2O_3 for the three phases are fully consistent with data already reported for RE-SOs. They also evidence that, despite the number of HP studies in bulk RE-SOs, there is a lack of high-quality HP-RS measurements for a number of bulk RE-SOs, especially for cations of similar size to Y, like Dy and Ho [111]. Therefore, the good agreement of our results on Y_2O_3 and other RE-SOs, suggest that the Raman modes of Dy_2O_3 and Ho_2O_3 should show a similar behavior at HP to those of Y_2O_3 and the same will apply to their pressure-induced PTs.

At this point, we want to comment that we have faced complications in simulating bulk B-type Y_2O_3 above 16 GPa. This is the reason of why theoretical lines in Fig. 4 have not been plotted beyond 22 GPa and that we do not trust calculations above 12 GPa, as previously commented. As observed in Fig. 4, theoretical lines corresponding to the Raman-active modes of the monoclinic phase show an anomalous pressure dependence above the range of 12–16 GPa. In particular, it is possible to observe that the lowest frequency A_g mode (initially at 113.6 cm^{-1}) gradually softens under pressure above 16 GPa. In order to ensure that this behavior is not associated with the presence of an imaginary phonon branch, the phonon dispersions and the respective density of states (DOS) were calculated for B-type Y_2O_3 at 0 GPa and 22.5 GPa. As can be seen in Fig. S10 in the SI, imaginary phonons do not appear at any of these pressures, thus confirming that this softness is not related to the presence of imaginary phonons. Therefore, we confirm that the monoclinic structure is dynamically stable at all calculated pressures. Consequently, the anomalies of the theoretical phonon frequencies

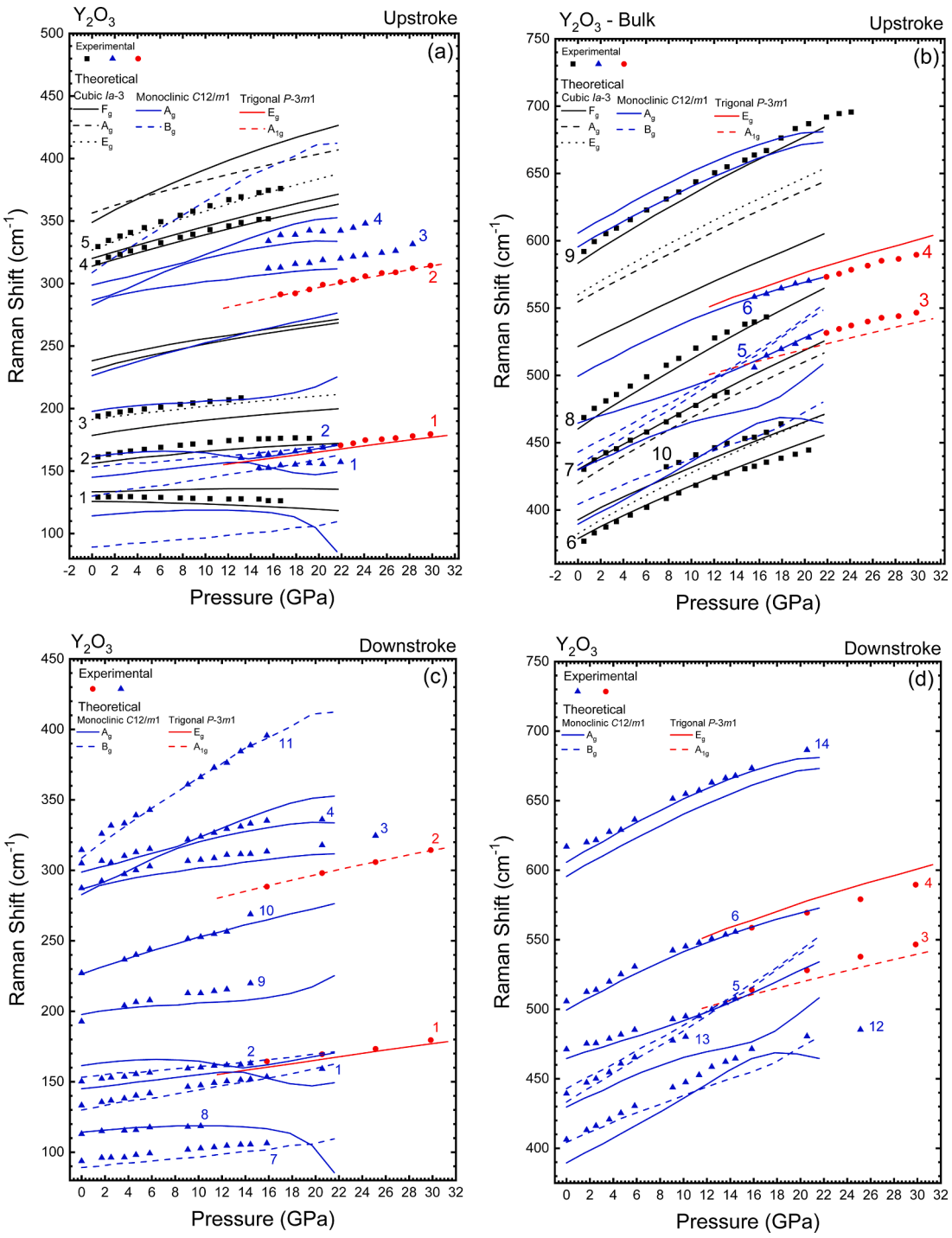

Fig. 4. Pressure dependence of the experimental (symbols) and theoretical (lines) Raman-active frequencies of bulk Y_2O_3 on the upstroke (a and b) and the downstroke (c and d). Black, blue, and red colors represent the cubic, monoclinic, and trigonal phases, respectively. The numbers correspond to the experimental peaks identified in Fig. 3. Error bars are smaller than the symbol size of each experimental point. (For interpretation of the references to color in this figure legend, the reader is referred to the web version of this article.)

above 12 GPa must be related to the anomalous values of the theoretical lattice parameters of the monoclinic structure above that pressure, as it has been previuosly commented. In this context, it should be stressed that monoclinic structures have a great number of degrees of freedom that could lead to a wrong optimisation of the structure during the relaxation procedure. Therefore, we speculate that it is possible that the origin of the anomalous values of some lattice parameters and vibrational frequencies in the monoclinic phase of Y_2O_3 above 12 GPa is related to relaxation problems of monoclinic phases due to the relatively large number of free parameters to be simultaneously relaxed.

A quantitative comparison of the experimental and theoretical frequencies and pressure coefficients for the C-, B-, and A-type phases of bulk Y_2O_3 is given in Table 3, Table 4, and Table 5, respectively. We must stress that we provide in this work both experimental and theoretical pressure coefficients for the Raman-active frequencies of the three phases of bulk Y_2O_3 that can be compared to the few existing data on this compound [19] and other RE-SOs, as recently reviewed [21]. The good correlation between the experimental and theoretical results

Table 3
Experimental (upstroke) and DFT-PBEsol theoretical zero-pressure frequencies (in cm^{-1}) and linear pressure coefficients (in cm^{-1}/GPa) for the Raman-active modes of C-type bulk Y_2O_3.

Symmetry	Experimental		Theoretical	
	ω_0	$d\omega/dP$	ω_0	$d\omega/dP$
F_g^1	129.8	−0.17	125.7	−0.34
F_g^2			133.4	0.11
A_g^1	162.0	1.05	156.1	0.74
F_g^3			178.5	0.97
E_g^1	194.2	1.10	191.2	0.92
F_g^4			230.6	1.73
F_g^5			238.2	1.50
F_g^6			313.9	2.29
F_g^7	317.8	2.32	320.1	2.37
E_g^2	329.9	3.09	326.8	2.81
F_g^8			348.9	3.57
A_g^2			356.4	2.31
F_g^9	377.4	3.91	378.8	3.51
E_g^3			382.4	4.10
F_g^{10}			392.7	3.58
A_g^3			419.7	4.47
F_g^{11}	430.3	4.49	430.1	4.42
F_g^{12}	468.1	5.02	460.3	4.80
F_g^{13}			521.4	3.86
A_g^4			554.6	4.11
E_g^4			560.0	4.30
F_g^{14}	592.3	4.87	583.4	4.63

Table 4
Experimental (downstroke) and DFT-PBEsol theoretical zero-pressure frequencies (in cm^{-1}) and linear pressure coefficients (in cm^{-1}/GPa) for the Raman-active modes of B-type bulk Y_2O_3. The pressure dependence of all frequencies has been fitted to a linear polynomial in the low-pressure range (0–12 GPa).

Symmetry	Experimental		Theoretical	
	ω_0	dω/dP	ω_0	$d\omega/dP$
B_g^1	94.2	0.81	89.2	0.77
A_g^1	113.6	0.52	114.2	0.37
B_g^2	133.7	1.31	130.0	1.40
A_g^2	–	–	145.0	1.00
B_g^3	150.8	0.89	153.2	0.72
A_g^3	–	–	161.5	0.08
A_g^4	196.5	1.65	197.7	0.71
A_g^5	228.4	2.38	226.3	2.54
A_g^6	290.3	1.68	282.8	1.58
A_g^7	–	–	286.7	3.33
A_g^8	302.9	2.07	298.8	2.53
B_g^4	314.5	4.93	308.7	5.58
A_g^9	405.9	4.15	389.5	4.69
B_g^5	–	–	404.3	3.30
A_g^{10}	–	–	429.7	3.39
B_g^6	440.3	4.10	433.3	5.12
B_g^7	–	–	443.0	4.60
A_g^{11}	471.0	2.30	464.6	2.73
A_g^{12}	506.0	3.87	499.4	4.06
A_g^{13}	613.6	3.95	595.5	4.36
A_g^{14}	–	–	605.7	4.44

supports the C-B-A PT sequence observed on the upstroke in bulk material and encourages us to propose the assignment of the nature of each peak of the three phases. In particular, a comparison of the pressure dependence of the strongest mode of the cubic phase and the theoretical modes allows us to confirm that this mode is an F_g mode and not a mixture of A_g and F_g modes, as previously assumed [56]. This result is in agreement with the assignment provided by Abrashev *et al.* who compared the zero-pressure frequencies of all C-type RE-SOs [59]. Further comparison of the pressure coefficients can be made with the data reported for other C-type, B-type, and A-type RE-SOs, as recently summarized [21]. Noteworthy, the strongest modes of B-type Y_2O_3 in our Raman spectra at room pressure correspond to the B_g modes, being the A_g modes much weaker. Similarly, the strongest mode of A-type Y_2O_3 is the E_g^1 mode near 170 cm^{-1} around 22 GPa that derives from one of the B_g modes of B-type Y_2O_3.

Table 5
Experimental (upstroke) and DFT-PBEsol theoretical frequencies (in cm^{-1}) and linear pressure coefficients (in cm^{-1}/GPa) for the Raman-active modes of A-type bulk Y_2O_3. The fits were performed from the pressure where the peaks are observed and the value of the frequency ω_{22GPa} corresponds to the pressure of 22 GPa.

Symmetry	Experimental		Theoretical	
	ω_{22GPa}	$d\omega/dP$	ω_{22GPa}	$d\omega/dP$
E_g^1	171.3	1.07	168.4	1.16
A_{1g}^1	300.9	1.81	300.5	1.71
A_{1g}^2	530.9	1.87	523.7	2.00
E_g^2	574.3	2.10	581.6	2.42

It must be finally stressed that the C-B-A PT sequence in bulk Y_2O_3 is supported by our theoretical calculations of the enthalpy of the three phases (Fig. 1(d)). It can be observed that the B-type phase becomes more stable than the C-type phase above 4.3 GPa and the A-type phase becomes competitive with respect to the B-type phase above 12.3 GPa. These theoretical results agree with previous enthalpy calculations [24,63] and with the recently published systematics of PTs in RE-SOs [20]. It must be noted that the experimental PT pressures are about 7–8 GPa higher than those theoretically predicted. The reason is in part due to the first-order and reconstructive nature of the C-B and B-A PTs; however, a larger discrepancy is expected for the C-B PT pressure than for the B-A PT pressure since the former has a larger relative volume change than the second, as recently reviewed [21]. In fact, laser-heating experiments have shown that when kinetic barriers are removed the C-B PT in bulk Y_2O_3 occurs around 2.9 GPa [24], which is much closer to the theoretical predictions.

In summary, HP-RS measurements on bulk Y_2O_3, interpreted with the help of lattice-dynamics calculations, evidence a pressure-induced C-B PT above 13 GPa and the appearance of the A-type phase above 16 GPa. The C-type phase completely disappears above 24 GPa and the B-type phase coexist with the A-type phase up to 28 GPa. On decreasing pressure, the A-B PT is observed below 16 GPa in good agreement with results upon increasing pressure and the metastable B-type phase is retained at room conditions. The results we have obtained for the PT sequence on upstroke are consistent with the results obtained from our HP-XRD measurements in bulk Y_2O_3 and with previous results of HP-RS measurements in bulk Y_2O_3. Therefore, we can conclude that the controversy about the appearance of the intermediate B-type phase (between the C- and A-type phases) on the upstroke in bulk Y_2O_3 has been put to an end. In this way, we have demonstrated that bulk Y_2O_3 shows the same behavior under compression as other RE-SOs of similar ionic radius than Y, such as Ho and Dy [80,81]. Additionally, we have provided a complete description of the vibrational properties of the three phases of bulk Y_2O_3 for its comparison with other RE-SOs.

To close the paper and help researchers to identify and understand the three polymorphs of Y_2O_3, we show in Fig. S11 in the SI the electronic band structure of: i) C-type bulk Y_2O_3 at 0 GPa; ii) A-type bulk Y_2O_3 at 23 GPa; and iii) B-type bulk Y_2O_3 at 0 and 22.5 GPa. The electronic band structure of C-type bulk Y_2O_3 at 0 GPa has a direct bandgap at Γ that is similar to those recently reported [112-114]. The electronic band structure of A-type bulk Y_2O_3 shows and indirect bandgap Γ-H that has not been previously reported to our knowledge, but our results for the DOS agree with those recently reported at different pressures [115]. Finally, the electronic band structure of B-type bulk Y_2O_3 at 0 GPa shows an indirect bandgap Γ-Y_2 that has not been previously reported to our knowledge; however, our results show that the direct bandgap at 0 GPa in B-type Y_2O_3 is slightly larger than that of C-type Y_2O_3. This result agrees with a recent report of the optical absorption properties of both

polymorphs [116].

Conclusions

We have reported a joint HP experimental and theoretical study of the structural and vibrational properties of bulk Y_2O_3. HP-XRD and HP-RS measurements have been interpreted with the help of theoretical *ab initio* calculations in order to solve some ongoing controversies regarding the pressure-induced PTs in C-type bulk Y_2O_3. Our study confirms the cubic (C-type)-monoclinic (B-type)-trigonal (A-type) PT sequence on the upstroke; thus, solving the issue of the presence of the B-type phase between the C- and A-type phase on the upstroke. On the downstroke, an A-B PT is observed and the B-type phase remains metastable at room pressure in good agreement with previous results. In this way, we conclude that the HP behavior of bulk Y_2O_3 we have found is fully consistent with what has been observed in HP studies of other RE-SOs with cations of similar ionic radii, such as Ho_2O_3 and Dy_2O_3.

Additionally, we have provided extensive theoretical structural data obtained from *ab initio* calculations regarding the behavior of the three observed phases of bulk Y_2O_3 under compression – an information not provided in the literature for most RE-SOs –. The theoretical structural data has allowed us to provide a detailed discussion of the structural behavior of the three phases of bulk Y_2O_3 under compression (unit-cell volumes, lattice parameters, free atomic parameters, Y-O bond distances, and polyhedral distortion indices). This information has allowed us to understand: i) the progressive increase in coordination along the pressure-induced C-B-A PT sequence, and ii) the general behavior of the C-, B-, and A-type structures under compression in bulk Y_2O_3. In this context, we have to mention that our theoretical results on the three phases of Y_2O_3 can be extrapolated to isostructural RE-SOs to understand their behavior under compression, since detailed structural information on the behavior of most bulk RE-SOs under compression has not been previously reported.

On the other hand, our HP-RS measurements on bulk Y_2O_3, interpreted with the help of theoretical lattice-dynamics calculations, have provided a much better characterization of the vibrational properties of bulk Y_2O_3 under compression than the only work reported to date. In this context, we have provided for the first time the experimental and theoretical frequencies and pressure coefficients of the Raman-active modes of the three known phases of Y_2O_3. Furthermore, we have shown that the good agreement between the experimental and calculated results for bulk Y_2O_3 has allowed us to provide a detailed assignment of the symmetry of the Raman-active modes of the C-, B-, and A-type phases of Y_2O_3. In particular, we have confirmed the F_g nature of the most intense Raman-active mode in C-type Y_2O_3.

Finally, we have provided the theoretical electronic band structure of the three phases of bulk Y_2O_3 at selected pressures. Our results for C-type bulk Y_2O_3 are in agreement with other calculations, while our results for B-type and A-type bulk Y_2O_3 are here shown for the first time to our knowledge.

All in all, we have clarified some previous issues regarding the behavior of bulk Y_2O_3 under compression by performing a joint experimental and theoretical work in which the results of two powerful experimental techniques, such as XRD and RS measurements, on the same sample have been interpreted with the help of state-of-the-art theoretical *ab initio* calculations [53]. We hope the present procedure will help other researchers to solve ongoing controversies, especially those still present in RE-SOs under compression.

CRediT authorship contribution statement

A.L.J. Pereira: Conceptualization, Writing – original draft, Formal analysis, Visualization. **J.A. Sans:** Formal analysis, Writing – review & editing, Investigation. **O. Gomis:** Investigation. **D. Santamaría-Pérez:** Writing – review & editing, Investigation. **S. Ray:** Writing – review & editing, Investigation. **A. Godoy-Jr:** Formal analysis, Writing – review & editing, Investigation. **A.S. da Silva-Sobrinho:** Writing – review & editing, Investigation. **P. Rodríguez-Hernández:** Formal analysis, Writing – review & editing, Investigation. **A. Muñoz:** Formal analysis, Writing – review & editing, Investigation. **C. Popescu:** Writing – review & editing, Investigation. **F.J. Manjón:** Conceptualization, Writing – review & editing, Supervision, Funding acquisition, Formal analysis, Resources.

Declaration of Competing Interest

The authors declare that they have no known competing financial interests or personal relationships that could have appeared to influence the work reported in this paper.

Data availability

Data will be made available on request.

Acknowledgements

This publication is part of the project MALTA Consolider Team network (RED2022-134388-T), financed by MINECO/AEI/10.13039/501100003329; by I + D + i projects PID2021-125927NB-C21 and PID2019-106383GB-42/43, financed by MCIN/AEI/10.13039/501100011033; by project CIPROM/2021/075 (GREENMAT), financed by Generalitat Valenciana; and by and Brazilian National Council for Scientific and Technological Development (CNPq), grants n^o 201050/2012-9 and 307199/2018-5. This study forms part of the Advanced Materials programme and was supported by MCIN with funding from European Union NextGenerationEU (PRTR-C17.I1) and by Generalitat Valenciana through project MFA/2022/025 (ARCANGEL). A. M., and P. R.-H. acknowledge computing time provided by Red Española de Supercomputación (RES) and MALTA-Cluster. We also thank DIAMOND and ALBA synchrotron light sources for funded experiments EE6073 and 2012100398 at the I15 and MSPD-BL04 beamlines, respectively. D. S.-P. acknowledge the financial support of MINECO, grant n^o PGC2018-097520-A-I00.

Appendix A. Supplementary data

Supplementary data to this article can be found online at https://doi.org/10.1016/j.rinp.2023.106499.

References

[1] Singh MK, Prakash A, Wolfowicz G, Wen J, Huang Y, Rajh T, et al. Epitaxial Er-doped Y_2O_3 on silicon for quantum coherent devices. APL Mater 2020;8(3):031111.
[2] Ukare RS, Kurzekar RR, Zade GD, Dhouble SJ. Yttrium Oxide As an Engineering Material. Int J Curr Eng Sci Res 2018;5:173–81.
[3] Verstegen JMPJ, Radielović D, Vrenken LE. A New Generation of "Deluxe" Fluorescent Lamps, Combining an Efficacy of 80 Lumens/W or More with a Color Rendering Index of Approximately 85. J Electrochem Soc 1974;121(12):1627.
[4] Konrad A, Fries T, Gahn A, Kummer F, Herr U, Tidecks R, et al. Chemical vapor synthesis and luminescence properties of nanocrystalline cubic Y_2O_3:Eu. J Appl Phys 1999;86(6):3129–33.
[5] Wakefield G, Holland E, Dobson PJ, Hutchison JL. Luminescence Properties of Nanocrystalline Y_2O_3:Eu. Adv Mater 2001;13:1557–60. https://doi.org/10.1002/1521-4095(200110)13:20<1557::AID-ADMA1557>3.0.CO;2-W.
[6] Igarashi T, Ihara M, Kusunoki T, Ohno K, Isobe T, Senna M. Relationship between optical properties and crystallinity of nanometer Y_2O_3: Eu phosphor. Appl Phys Lett 2000;76:1549–51. https://doi.org/10.1063/1.126092.
[7] Qi Z, Shi C, Zhang W, Zhang W, Hu T. Local structure and luminescence of nanocrystalline Y_2O_3:Eu. Appl Phys Lett 2002;81:2857–9. https://doi.org/10.1063/1.1513659.
[8] Boukerika A, Guerbous L. Annealing effects on structural and luminescence properties of red Eu^{3+}-doped Y_2O_3 nanophosphors prepared by sol-gel method. J Lumin 2014;145:148–53. https://doi.org/10.1016/j.jlumin.2013.07.037.
[9] Yoo HS, Jang HS, Bin IW, Kang JH, Jeon DY. Particle size control of a monodisperse spherical Y_2O_3: Eu^{3+} phosphor and its photoluminescence properties. J Mater Res 2007;22:2017–24. https://doi.org/10.1557/jmr.2007.0257.

[10] Hoekstra HR. Phase Relationships in the Rare Earth Sesquioxides at High Pressure. Inorg Chem 1966;5:754–7. https://doi.org/10.1021/ic50039a013.

[11] Hoekstra HR, Gingerich KA. High-Pressure B-Type Polymorphs of Some Rare-Earth Sesquioxides. Science (80-) 1964;146(3648):1163–4.

[12] Skrikanth V, Sato A, Yoshimoto J, Kim JH, Ikegami T. Synthesis and crystal structure study of Y_2O_3 high-pressure polymorph. Cryst Res Technol 1994;29:981–4. https://doi.org/10.1002/crat.2170290712.

[13] Deutsch S, Al-Sharab JF, Kear BH, Tse SD, Voronov OA, Nordahl CS. Directional crystallization of columnar-grained monoclinic Y_2O_3 under high pressure. Scr Mater 2013;69:651–3. https://doi.org/10.1016/j.scriptamat.2013.07.021.

[14] Zhang Q, Wu X, Ovsyannikov SV, Dong J, Qin S, Dubrovinsky LS, et al. High-pressure, high-temperature synthesis and properties of the monoclinic phase of Y_2O_3. Chem Res Chinese Univ 2016;32(4):545–8.

[15] Li X, Xia X, Xu H, Zhong S, He D. High-temperature high pressure synthesis of monoclinic Y_2O_3. Mater Lett 2019;239:82–5. https://doi.org/10.1016/j.matlet.2018.12.068.

[16] Gaboriaud RJ, Jublot M, Paumier F, Lacroix B. Phase transformations in Y_2O_3 thin films under swift Xe ions irradiation. Nucl Instruments Methods Phys Res Sect B Beam Interact with Mater Atoms 2013;310:6–9. https://doi.org/10.1016/j.nimb.2013.05.014.

[17] Lee MK, Park EK, Park JJ, Rhee CK. Control of Y_2O_3 phase and its nanostructure formation through a very high energy mechanical milling. J Solid State Chem 2013;201:56–62. https://doi.org/10.1016/j.jssc.2013.02.011.

[18] Zinkevich M. Thermodynamics of rare earth sesquioxides. Prog Mater Sci 2007;52:597–647. https://doi.org/10.1016/j.pmatsci.2006.09.002.

[19] Husson E, Proust C, Gillet P, Itié JP. Phase transitions in yttrium oxide at high pressure studied by Raman spectroscopy. Mater Res Bull 1999;34:2085–92. https://doi.org/10.1016/S0025-5408(99)00205-6.

[20] Manjón FJ, Tresserras JAS, Ibáñez J, Pereira ALJ. Pressure-induced phase transitions in sesquioxides. Crystals 2019;9:1–31. https://doi.org/10.3390/cryst9120630.

[21] Ibáñez J, Sans JÁ, Cuenca-Gotor V, Oliva R, Gomis Ó, Rodríguez-Hernández P, et al. Structural and Lattice-Dynamical Properties of Tb_2O_3 under Compression: A Comparative Study with Rare Earth and Related Sesquioxides. Inorg Chem 2020;59(14):9648–66.

[22] Wang L, Pan Y, Ding Y, Yang W, Mao WL, Sinogeikin SV, et al. High-pressure induced phase transitions of Y_2O_3 and Y_2O_3:Eu^{3+}. Appl Phys Lett 2009;94(6):061921.

[23] Wang L, Yang W, Ding Y, Ren Y, Xiao S, Liu B, et al. Size-dependent amorphization of nanoscale Y_2O_3 at high pressure. Phys Rev Lett 2010;105:1–4. https://doi.org/10.1103/PhysRevLett.105.095701.

[24] Yusa H, Tsuchiya T, Sata N, Ohishi Y. Dense Yttria Phase Eclipsing the A-Type Sesquioxide Structure: High-Pressure Experiments and ab initio Calculations. Inorg Chem 2010;49:4478–85. https://doi.org/10.1021/ic100042z.

[25] Halevy I, Carmon R, Winterrose ML, Yeheskel O, Tiferet E, Ghose S. Pressure-induced structural phase transitions in Y_2O_3 sesquioxide. J Phys Conf Ser 2010;215:012003. https://doi.org/10.1088/1742-6596/215/1/012003.

[26] Zhu H, Ma Y, Yang H, Zhu P, Du J, Ji C, et al. Ultrastable structure and luminescence properties of Y_2O_3 nanotubes. Solid State Commun 2010;150(27-28):1208–12.

[27] Dai RC, Zhang ZM, Zhang CC, Ding ZJ. Photoluminescence and Raman Studies of Y_2O_3:Eu^{3+} Nanotubes Under High Pressure. J Nanosci Nanotechnol 2010;10:7629–33. https://doi.org/10.1166/jnn.2010.2752.

[28] Dai R, Wang Z, Zhang Z, Ding Z. Photoluminescence study of SiO_2 coated Eu^{3+}:Y_2O_3 core-shells under high pressure. J Rare Earths 2010;28:241–5. https://doi.org/10.1016/S1002-0721(10)60275-X.

[29] Kear BH, Al-Sharab JF, Sadangi RK, Deutsch S, Kavukcuoglu NB, Tse SD, et al. On the Conversion of Bulk Polycrystalline Y_2O_3 into the Nanocrystalline State. J Am Ceram Soc 2011;94(6):1744–6.

[30] Bose PP, Gupta MK, Mittal R, Rols S, Achary SN, Tyagi AK, et al. Phase transitions and thermodynamic properties of yttria, Y2O3: Inelastic neutron scattering shell model and first-principles calculations. Phys Rev B 2011;84:094301. https://doi.org/10.1103/PhysRevB.84.094301.

[31] Bose PP, Gupta MK, Mittal R, Rols S, Achary SN, Tyagi AK, et al. High pressure phase transitions in yttria, Y_2O_3. J Phys Conf Ser 2012;377:10–3. https://doi.org/10.1088/1742-6596/377/1/012036.

[32] Srivastava AM, Renero-Lecuna C, Santamaría-Pérez D, Rodríguez F, Valiente R. Pressure-induced Pr^{3+} 3P0 luminescence in cubic Y_2O_3. J Lumin 2014;146:27–32. https://doi.org/10.1016/j.jlumin.2013.09.028.

[33] Zhang J, Cui H, Zhu P, Ma C, Wu X, Zhu H, et al. Photoluminescence studies of Y_2O_3:Eu^3 under high pressure. J Appl Phys 2014;115(2):023502.

[34] Li Z, Wang J, Wang L, Bai X, Song H, Zhou Q, et al. The pressure induced amorphization and behavior of octahedron in Y_2O_3/Eu^{3+} nanotubes. Mater Res Express 2014;1(2):025013.

[35] Li Z, Wang J, Hou Y, Bai X, Song H, Zhou Q, et al. Analysis of the upconversion photoluminescence spectra as a probe of local microstructure in Y_2O_3/Eu^{3+} nanotubes under high pressure. RSC Adv 2015;5(5):3130–4.

[36] Kishimura H, Hamada S, Aruga A, Matsumoto H. Photoluminescence studies of shock-recovered Y_2O_3:Eu^{3+}. Appl Phys Lett 2015;106(1):011903.

[37] Kishimura H, Hamada S, Aruga A, Matsumoto H. Effect of shock compression on optical and structural properties of Eu2O3 and Y_2O_3:Eu^{3+} powders. J Appl Phys 2016;119(20):205111.

[38] Dilawar Sharma N, Singh J, Vijay A, Samanta K, Dogra S, Bandyopadhyay AK. Pressure-Induced Structural Transition Trends in Nanocrystalline Rare-Earth Sesquioxides: A Raman Investigation. J Phys Chem C 2016;120:11679–89. https://doi.org/10.1021/acs.jpcc.6b02104.

[39] Li Z, Xu H, Liu Bo, Song Q, Zhou Q, Song H, et al. Investigation of the lattice behavior of cubic Y_2O_3/Eu^{3+} nanotubes under high pressure. Phys Status Solidi Basic Res 2016;253(11):2204–8.

[40] Wang J-H, Li Z-P, Liu Bo, Liu B-B. Local microstructural analysis for Y_2O_3/Eu^{3+}/Mg^{2+} nanorods by Raman and photoluminescence spectra under high pressure. Chinese Phys B 2017;26(2):026101.

[41] Zhang Q, Wu X, Qin S. Pressure-induced phase transition of B-type Y_2O_3. Chinese Phys B 2017;26(9):090703.

[42] Sawyer JO, Hyde BG, Eyring L. Pressure and Polymorphism in the Rare Earth Sesquioxides. Inorg Chem 1965;4:426–7. https://doi.org/10.1021/ic50025a043.

[43] Atou T, Kusaba K, Fukuoka K, Kikuchi M, Syono Y. Shock-induced phase transition of M_2O_3 (M = Sc, Y, Sm, Gd, and In)-type compounds. J Solid State Chem 1990;89:378–84. https://doi.org/10.1016/0022-4596(90)90280-B.

[44] Jovanic BR, Radenkovic B, Zekovic LD. The effect of pressure on the position and fluorescence lifetime for the the 5D0 → 7F2 transition in $Y_{1.9}Eu_{0.1}O_3$. J Phys Condens Matter 1996;8:4107–10. https://doi.org/10.1088/0953-8984/8/22/014.

[45] Dilawar N, Varandani D, Mehrotra S, Poswal HK, Sharma SM, Bandyopadhyay AK. Anomalous high pressure behaviour in nanosized rare earth sesquioxides. Nanotechnology 2008;19(11):115703.

[46] Jovanic BR, Dramicanin M, Viana B, Panic B, Radenkovic B. High-pressure optical studies of Y_2O_3:Eu^{3+} nanoparticles. Radiat Eff Defects Solids 2008;163:925–31. https://doi.org/10.1080/10420150802082705.

[47] Bai X, Song HW, Liu BB, Hou YY, Pan GH, Ren XG. Effects of High Pressure on the Luminescent Properties of Nanocrystalline and Bulk Y_2O_3:Eu^{3+}. J Nanosci Nanotechnol 2008;8:1404–9. https://doi.org/10.1166/jnn.2008.351.

[48] Mcclure JP. High pressure phase transistions in the lanthanide sesquioxides. University of Nevada; 2009.

[49] Jiang S, Liu J, Li X-D, Li Y-C, He S-M, Zhang J-C. High-Pressure Phase Transitions of Cubic Y_2O_3 under High Pressures by In-situ Synchrotron X-Ray Diffraction. Chinese Phys Lett 2019;36(4):046103.

[50] García-Domene B, Sans JA, Gomis O, Manjón FJ, Ortiz HM, Errandonea D, et al. Pbca-type In_2O_3: The high-pressure post-corundum phase at room temperature. J Phys Chem C 2014;118(35):20545–52.

[51] García-Domene B, Sans JA, Manjón FJ, Ovsyannikov SV, Dubrovinsky LS, Martinez-Garcia D, et al. Synthesis and High-Pressure Study of Corundum-Type In_2O_3. J Phys Chem C 2015;119(52):29076–87.

[52] Gallego-Parra S, Vilaplana R, Gomis O, Lora da Silva E, Otero-de-la-Roza A, Rodríguez-Hernández P, et al. Structural, vibrational and electronic properties of α′-Ga_2S_3 under compression. PCCP 2021;23(11):6841–62.

[53] Manjón FJ, Sans JÁ, Rodríguez-Hernández P, Muñoz A. Combined Experimental and Theoretical Studies: Lattice-Dynamical Studies at High Pressures with the Help of Ab Initio Calculations. Minerals 2021;11:1283. https://doi.org/10.3390/min11111283.

[54] Schaack G, Koningstein JA. Phonon and Electronic Raman Spectra of Cubic Rare-Earth Oxides and Isomorphous Yttrium Oxide*. J Opt Soc Am 1970;60:1110. https://doi.org/10.1364/JOSA.60.001110.

[55] White WB, Keramidas VG. Vibrational spectra of oxides with the C-type rare earth oxide structure. Spectrochim Acta Part A Mol Spectrosc 1972;28:501–9. https://doi.org/10.1016/0584-8539(72)80237-X.

[56] Repelin Y, Proust C, Husson E, Beny JM. Vibrational Spectroscopy of the C-Form of Yttrium Sesquioxide. J Solid State Chem 1995;118:163–9. https://doi.org/10.1006/jssc.1995.1326.

[57] Ubaldini A, Carnasciali MM. Raman characterisation of powder of cubic RE_2O_3 (RE=Nd, Gd, Dy, Tm, and Lu), Sc_2O_3 and Y_2O_3. J Alloy Compd 2008;454:374–8. https://doi.org/10.1016/j.jallcom.2006.12.067.

[58] Dilawar N, Mehrotra S, Varandani D, Kumaraswamy BV, Haldar SK, Bandyopadhyay AK. A Raman spectroscopic study of C-type rare earth sesquioxides. Mater Charact 2008;59:462–7. https://doi.org/10.1016/j.matchar.2007.04.008.

[59] Abrashev MV, Todorov ND, Geshev J. Raman spectra of R_2O_3 (R—rare earth) sesquioxides with C-type bixbyite crystal structure: A comparative study. J Appl Phys 2014;116(10):103508.

[60] Xu Y-N, Gu Z, Ching WY. Electronic, structural, and optical properties of crystalline yttria. Phys Rev B 1997;56:14993–5000. https://doi.org/10.1103/PhysRevB.56.14993.

[61] Hirosaki N, Ogata S, Kocer C. Ab initio calculation of the crystal structure of the lanthanide Ln_2O_3 sesquioxides. J Alloy Compd 2003;351:31–4. https://doi.org/10.1016/S0925-8388(02)01043-5.

[62] Wu B, Zinkevich M, Wang C, Aldinger F. Ab initio energetic study of oxide ceramics with rare-earth elements. Rare Met 2006;25:549–55. https://doi.org/10.1016/S1001-0521(06)60097-1.

[63] Wu B, Zinkevich M, Aldinger F, Wen D, Chen L. Ab initio study on structure and phase transition of A- and B-type rare-earth sesquioxides Ln_2O_3 (Ln=La–Lu, Y, and Sc) based on density function theory. J Solid State Chem 2007;180:3280–7. https://doi.org/10.1016/j.jssc.2007.09.022.

[64] Badehian HA, Salehi H, Ghoohestani M, Ching W-Y. First-Principles Study of Elastic, Structural, Electronic, Thermodynamical, and Optical Properties of Yttria (Y_2O_3) Ceramic in Cubic Phase. J Am Ceram Soc 2013;96(6):1832–40.

[65] Zhang X, Gui W, Zeng Q. First-principles study of structural, mechanical, and thermodynamic properties of cubic Y_2O_3 under high pressure. Ceram Int 2017;43:3346–55. https://doi.org/10.1016/j.ceramint.2016.11.176.

[66] Li D, Zhang X, Liu C, Wang F, Zhang H, Tian M. Insight into the pressure effect on the structural stability and physical properties of cubic sesquioxides X_2O_3 (X= Sc, Y and In). Vacuum 2019;168:108855. https://doi.org/10.1016/j.vacuum.2019.108855.

[67] Fauth F, Peral I, Popescu C, Knapp M. The new Material Science Powder Diffraction beamline at ALBA Synchrotron. Powder Diffr 2013;28:S360–70. https://doi.org/10.1017/S0885715613000900.

[68] Merrill L, Bassett WA. Miniature diamond anvil pressure cell for single crystal x-ray diffraction studies. Rev Sci Instrum 1974;45:290–4. https://doi.org/10.1063/1.1686607.

[69] Dewaele A, Loubeyre P, Mezouar M. Equations of state of six metals above 94 GPa. Phys Rev B – Condens Matter Mater Phys 2004;70:1–8. https://doi.org/10.1103/PhysRevB.70.094112.

[70] Prescher C, Prakapenka VB. DIOPTAS: A program for reduction of two-dimensional X-ray diffraction data and data exploration. High Press Res 2015;35:223–30. https://doi.org/10.1080/08957959.2015.1059835.

[71] Rodríguez-Carvajal J. Recent advances in magnetic structure determination by neutron powder diffraction. Phys B Phys Condens Matter 1993;192:55–69. https://doi.org/10.1016/0921-4526(93)90108-I.

[72] Nolze G, Kraus W. PowderCell 2.0 for Windows. Powder Diffr 2016;13(4):256–9.

[73] Mao HK, Xu J, Bell PM. Calibration of the ruby pressure gauge to 800 kbar under quasi-hydrostatic conditions. J Geophys Res 1986;91:4673. https://doi.org/10.1029/JB091iB05p04673.

[74] Errandonea D, Muñoz A, Gonzalez-Platas J. Comment on High-pressure x-ray diffraction study of YBO_3/Eu^{3+}, $GdBO_3$, and $EuBO_3$: Pressure-induced amorphization in $GdBO_3$. J Appl Phys 2014;115:113–6. https://doi.org/10.1063/1.4881057.

[75] Hohenberg P, Kohn W. Inhomogeneous Electron Gas. Phys Rev 1964;136:B864–71. https://doi.org/10.1103/PhysRev.136.B864.

[76] Kresse G, Furthmüller J. Efficiency of ab-initio total energy calculations for metals and semiconductors using a plane-wave basis set. Comput Mater Sci 1996;6:15–50. https://doi.org/10.1016/0927-0256(96)00008-0.

[77] Kresse G, Furthmüller J. Efficient iterative schemes for ab initio total-energy calculations using a plane-wave basis set. Phys Rev B 1996;54:11169–86. https://doi.org/10.1103/PhysRevB.54.11169.

[78] Blöchl PE. Projector augmented-wave method. Phys Rev B 1994;50:17953–79. https://doi.org/10.1103/PhysRevB.50.17953.

[79] Kresse G, Joubert D. From ultrasoft pseudopotentials to the projector augmented-wave method. Phys Rev B - Condens Matter Mater Phys 1999;59(3):1758–75.

[80] Perdew JP, Ruzsinszky A, Csonka GI, Vydrov OA, Scuseria GE, Constantin LA, et al. Restoring the Density-Gradient Expansion for Exchange in Solids and Surfaces. Phys Rev Lett 2008;100(13):136406. https://doi.org/10.1103/PhysRevLett.100.136406.

[81] Monkhorst HJ, Pack JD. Special points for Brillouin-zone integrations. Phys Rev B 1976;13:5188–92. https://doi.org/10.1103/PhysRevB.13.5188.

[82] Parlinski K, Li ZQ, Kawazoe Y. First-Principles Determination of the Soft Mode in Cubic ZrO_2. Phys Rev Lett 1997;78:4063–6. https://doi.org/10.1103/PhysRevLett.78.4063.

[83] Jiang S, Liu J, Li X, Bai L, Xiao W, Zhang Y, et al. Phase transformation of Ho_2O_3 at high pressure. J Appl Phys 2011;110(1):013526.

[84] Jiang S, Liu J, Lin C, Bai L, Zhang Y, Li X, et al. Structural transformations in cubic Dy_2O_3 at high pressures. Solid State Commun 2013;169:37–41.

[85] Gomis O, Sans JA, Lacomba-Perales R, Errandonea D, Meng Y, Chervin JC, et al. Complex high-pressure polymorphism of barium tungstate. Phys Rev B – Condens Matter Mater Phys 2012;86:1–10. https://doi.org/10.1103/PhysRevB.86.054121.

[86] Pereira ALJ, Errandonea D, Beltrán A, Gracia L, Gomis O, Sans JA, et al. Structural study of α-Bi_2O_3 under pressure. J Phys Condens Matter 2013;25(47):475402.

[87] Santamaría-Pérez D, Gracia L, Garbarino G, Beltrán A, Chuliá-Jordán R, Gomis O, et al. High-pressure study of the behavior of mineral barite by x-ray diffraction. Phys Rev B – Condens Matter Mater Phys 2011;84(5). https://doi.org/10.1103/PhysRevB.84.054102.

[88] Errandonea D, Meng Y, Somayazulu M, Häusermann D. Pressure-induced α → ω transition in titanium metal: A systematic study of the effects of uniaxial stress. Phys B Condens Matter 2005;355:116–25. https://doi.org/10.1016/j.physb.2004.10.030.

[89] Tropf WJ, Harris DC. Mechanical, Thermal, And Optical Properties Of Yttria And Lanthana-Doped Yttria. In: Klocek P, editor. Wind. Dome Technol. Mater., 1989, p. 9. https://doi.org/10.1117/12.960758.

[90] Yeheskel O, Tevet O. Elastic Moduli of Transparent Yttria. J Am Ceram Soc 2004;82:136–44. https://doi.org/10.1111/j.1151-2916.1999.tb01733.x.

[91] Palko JW, Kriven WM, Sinogeikin SV, Bass JD, Sayir A. Elastic constants of yttria (Y_2O_3) monocrystals to high temperatures. J Appl Phys 2001;89:7791–6. https://doi.org/10.1063/1.1369395.

[92] Birch F. Finite strain isotherm and velocities for single-crystal and polycrystalline NaCl at high pressures and 300°K. J Geophys Res 1978;83:1257. https://doi.org/10.1029/JB083iB03p01257.

[93] Rahm M, Skorodumova NV. Phase stability of the rare-earth sesquioxides under pressure. Phys Rev B 2009;80:104105. https://doi.org/10.1103/PhysRevB.80.104105.

[94] Richard D, Errico LA, Rentería M. Structural properties and the pressure-induced C → A phase transition of lanthanide sesquioxides from DFT and DFT + U calculations. J Alloy Compd 2016;664:580–9. https://doi.org/10.1016/j.jallcom.2015.12.236.

[95] Wu B, Zinkevich M, Aldinger F, Wen D, Chen L. Ab initio study on structure and phase transition of A- and B-type rare-earth sesquioxides Ln_2O_3 (Ln=La-Lu, Y, and Sc) based on density function theory. J Solid State Chem 2007;180:3280–7. https://doi.org/10.1016/j.jssc.2007.09.022.

[96] Cuenca-Gotor VP, Sans JA, Ibáñez J, Popescu C, Gomis O, Vilaplana R, et al. Structural, Vibrational, and Electronic Study of α-As_2Te_3 under Compression. J Phys Chem C 2016;120(34):19340–52.

[97] Haussühl S. Physical Properties of Crystals - An Introduction. KGaA: WILEY-VCH Verlag GmbH & Co; 2007.

[98] Angel RJ. Win_Strain n.d. http://www.rossangel.com/text_strain.htm (accessed December 16, 2022).

[99] Momma K, Izumi F. VESTA 3 for three-dimensional visualization of crystal, volumetric and morphology data. J Appl Cryst 2011;44:1272–6. https://doi.org/10.1107/S0021889811038970.

[100] Williams DK, Bihari B, Tissue BM, McHale JM. Preparation and Fluorescence Spectroscopy of Bulk Monoclinic Eu^{3+} :Y_2O_3 and Comparison to Eu^{3+}:Y_2O_3 Nanocrystals. J Phys Chem B 1998;102:916–20. https://doi.org/10.1021/jp972996e.

[101] Irshad KA, Anees P, Sahoo S, Sanjay Kumar NR, Srihari V, Kalavathi S, et al. Pressure induced structural phase transition in rare earth sesquioxide Tm_2O_3: Experiment and ab initio calculations. J Appl Phys 2018;124(15):155901.

[102] Zarembowitch J, Gouteron J, Lejus AM. Raman spectrum of single crystals of monoclinic B-type gadolinium sesquioxide. J Raman Spectrosc 1980;9:263–5. https://doi.org/10.1002/jrs.1250090410.

[103] Jiang S, Liu J, Lin C, Bai L, Xiao W, Zhang Y, et al. Pressure-induced phase transition in cubic Lu_2O_3. J Appl Phys 2010;108(8):083541.

[104] Lin CM, Te WK, Hung TL, Sheu HS, Tsai MH, Lee JF, et al. Phase transitions in Lu_2O_3 under high pressure. Solid State Commun 2010;150:1564–9. https://doi.org/10.1016/j.ssc.2010.05.046.

[105] Pandey SD, Samanta K, Singh J, Sharma ND, Bandyopadhyay AK. Anharmonic behavior and structural phase transition in Yb_2O_3. AIP Adv 2013;3(12):122123.

[106] Ovsyannikov SV, Bykova E, Bykov M, Wenz MD, Pakhomova AS, Glazyrin K, et al. Structural and vibrational properties of single crystals of Scandia, Sc_2O_3 under high pressure. J Appl Phys 2015;118(16):165901.

[107] Garcia-Domene B, Ortiz HM, Gomis O, Sans JA, Manjón FJ, Muñoz A, et al. High-pressure lattice dynamical study of bulk and nanocrystalline In2O3. J Appl Phys 2012;112(12):123511.

[108] Jiang S, Liu J, Lin C, Li X, Li Y. High-pressure x-ray diffraction and Raman spectroscopy of phase transitions in Sm_2O_3. J Appl Phys 2013;113(11):113502.

[109] Hongo T, Kondo KI, Nakamura KG, Atou T. High pressure Raman spectroscopic study of structural phase transition in samarium oxide. J Mater Sci 2007;42:2582–5. https://doi.org/10.1007/s10853-006-1417-5.

[110] Jiang S, Liu J, Bai L, Li X, Li Y, He S, et al. Anomalous compression behaviour in Nd_2O_3 studied by x-ray diffraction and Raman spectroscopy. AIP Adv 2018;8(2):025019.

[111] Lonappan D, Shekar NVC, Ravindran TR, Sahu PC. High-pressure phase transition in Ho_2O_3. Mater Chem Phys 2010;120:65–7. https://doi.org/10.1016/j.matchemphys.2009.10.022.

[112] Ahuja BL, Sharma S, Heda NL, Tiwari S, Kumar K, Meena BS, et al. Electronic and optical properties of ceramic Sc_2O_3 and Y_2O_3: Compton spectroscopy and first principles calculations. J Phys Chem Solid 2016;92:53–63.

[113] Zeng W, Liu QJ, Liu ZT. Structural, electronic, and optical properties of cubic Y_2O_3: First-principles calculations. Mosc Univ Phys Bull 2018;73:95–100. https://doi.org/10.3103/S0027134918010162.

[114] Naveed-Ul-Haq M. Theoretical Studies of Electronic and Optical Properties of Bixbyite and Fluorite Polymorphs of Sb-Doped Y_2O_3. J Electron Mater 2021;50:6784–94. https://doi.org/10.1007/s11664-021-09185-z.

[115] Li YF, Xiao B, Sun L, Gao YM, Ma SQ, Yi DW. Pressure dependence of thermal physical properties of A-type R_2O_3 (R=Y, La): A first-principles study. J Phys Chem Solid 2017;103:49–58. https://doi.org/10.1016/j.jpcs.2016.12.001.

[116] Boukhvalov DW, Zatsepin DA, Kuznetsova YA, Gavrilov NV, Zatsepin AF. Comparative analysis of the electronic energy structure of nanocrystalline polymorphs of Y_2O_3 thin Layers: Theory and experiments. Appl Surf Sci 2023;613:155935. https://doi.org/10.1016/j.apsusc.2022.155935.